A New Type of Jovian Hectometric Radiation Powered by Monoenergetic Electron Beams

Brieuc Collet, L. Lamy, C. Louis, P. Zarka, R. Prangé, P. Louarn, W. Kurth, F. Allegrini

To cite this version:

Brieuc Collet, L. Lamy, C. Louis, P. Zarka, R. Prangé, et al.. A New Type of Jovian Hectometric Radiation Powered by Monoenergetic Electron Beams. Journal of Geophysical Research Space Physics, 2024, 129 (5), 10.1029/2024JA032422 . hal-04584701

HAL Id: hal-04584701
https://hal.science/hal-04584701

Submitted on 24 May 2024

JGR Space Physics

RESEARCH ARTICLE
10.1029/2024JA032422

Key Points:

- A survey of Juno/Waves in situ measurement (2016–2022) reveals 15 hectometric sources observed below the local electron cyclotron frequency
- We show with a Cyclotron Maser Instability growth rate analysis using Juno/JADE-E data that they are generated by 0.2–5 keV shell electrons
- This new source of Jovian auroral radio emission is reminiscent of the auroral kilometric radiations of Earth and Saturn

Supporting Information:

Supporting Information may be found in the online version of this article.

Correspondence to:

B. Collet,
brieuc.collet@lam.fr

Citation:

Collet, B., Lamy, L., Louis, C. K., Zarka, P., Prangé, R., Louarn, P., et al. (2024). A new type of Jovian hectometric radiation powered by monoenergetic electron beams. *Journal of Geophysical Research: Space Physics*, *129*, e2024JA032422. https://doi.org/10.1029/2024JA032422

Received 5 JAN 2024
Accepted 14 APR 2024

A New Type of Jovian Hectometric Radiation Powered by Monoenergetic Electron Beams

B. Collet[1], L. Lamy[1,2], C. K. Louis[2], P. Zarka[2], R. Prangé[2], P. Louarn[3], W. S. Kurth[4], and F. Allegrini[5,6]

[1]Aix Marseille University, CNRS, CNES, LAM, Marseille, France, [2]LESIA, Observatoire de Paris, PSL, CNRS, SU/UPMC, UPD, Meudon, France, [3]IRAP, Université de Toulouse, CNRS, CNES, UPS, Toulouse, France, [4]Department of Physics and Astronomy, University of Iowa, Iowa City, IA, USA, [5]Southwest Research Institute, San Antonio, TX, USA, [6]Department of Physics and Astronomy, University of Texas at San Antonio, San Antonio, TX, USA

Abstract In this study, we statistically analyze the Jovian auroral radio sources detected in situ by Juno/Waves at frequencies f below the electron cyclotron frequency f_{ce}. We first conduct a survey of Juno/Waves data over 1–40 MHz from 2016 to 2022. The 15 detected HectOMetric (HOM) sources all lie within 1–5 MHz and are both less frequent than the radio sources commonly observed slightly above f_{ce} and clustered in the southern hemisphere, within ~90–270° longitudes. We analyze these emission regions with a growth rate analysis in the framework of the Cyclotron Maser Instability (CMI), which we apply to JADE-E high cadence electron measurements. We show that the $f < f_{ce}$ emissions correspond to crossed radio sources, ~300 km wide. They are located in a hot and highly depleted auroral plasma environment, along flux tubes colocated with upward field-aligned current and at the equatorward edge of the main auroral oval. The wave amplification is consistent with the CMI and its free energy source consists of a shell-type electron distribution function (EDF) with characteristic energies of 0.2–5keV. More energetic, 5–50 keV, shell-type EDFs were systematically observed at higher latitudes but without any radio counterpart. Various parameters for the $f < f_{ce}$ HOM sources, reminiscent of the ones at Earth/Saturn, are compared. Other CMI-unstable EDFs, primarily loss cone ones, are systematically observed during the same intervals, giving rise to emission observed at $f_{ce} < f < f_{ce} + 0.5\%$. Our analysis thus reveals that different portions of the same EDF can be CMI-unstable and simultaneously amplify radio waves below and above f_{ce}.

Plain Language Summary Taking advantage of Juno radio, electron and magnetic measurements within the source of Jupiter's auroral radio emissions, we analyze a new type of HectOMectric (HOM, a wavelength of 1 hm matching a frequency of 3 MHz) emissions observed in situ by Juno/Waves at frequencies f below the electron cyclotron frequency f_{ce}. We first survey the Juno/Waves radio observations over 1–40 MHz between 2016 and 2022, covering the first 45 orbits. The 15 detected cases of $f < f_{ce}$ emissions are much less frequent than the usual HOM emissions observed slightly above f_{ce} and their sources are inhomogeneously distributed. We then analyze these events in the framework of the Cyclotron Maser Instability (CMI) by calculating their theoretical growth rate from electron distribution functions simultaneously measured by the Juno/JADE-E spectrometer. We show that the $f < f_{ce}$ HOM sources are definitely consistent with the CMI powered by electron beams of 0.2–5 keV. This new type of Jovian auroral radio emission is reminiscent of the ones prominently observed at Earth and Saturn. These $f < f_{ce}$ sources co-exist with HOM emission at $f_{ce} < f < f_{ce} + 0.5\%$, which is also driven by the CMI based on different well-known sources of free energy.

1. Introduction

Jupiter is the brightest planetary radio emitter in the solar system. The auroral regions of its magnetosphere radiate intense, non thermal, radio emissions at frequencies ranging from a few kHz to 40 MHz. This spectral range encompasses various radio components, which have been historically classified by wavelength as DecAMetric (DAM, ~10–40 MHz), HectOMetric (HOM, ~500 kHz–10 MHz), and broadband-KilOMetric (bKOM, a few kHz up to 1 MHz) (Zarka, 1998, and references therein). These emissions, the most intense of which are induced by Io, are produced at frequencies close to the electron cyclotron frequency $f_{ce} = \frac{eB}{2\pi m_e}$ (with e and m_e the electron charge and mass, B the magnetic field amplitude). They are beamed along a thin hollow-cone at large angles from the local magnetic field, which is responsible for the arc-shaped structures observed in time-frequency radio spectrograms, they propagate in the Right-handed eXtraordinary (R-X) mode and are associated with the powerful Jovian aurorae. They were thus early suspected to be driven by energetic auroral electrons through the Cyclotron Master Instability (CMI).

This electron-wave resonant instability was first proposed by Wu and Lee (1979) to account for Auroral Kilometric Radiation (AKR) at Earth. It amplifies waves at frequencies close to f_{ce} in low density plasma regions where $f_{pe} \ll f_{ce}$, with f_{pe} the electron plasma frequency (proportional to $\sqrt{n_e}$, with n_e the electron density) from a weakly relativistic, out-of-equilibrium, Electron Distribution Function (EDF). The AKR free energy source was first thought to reside in the loss cone portion of the auroral EDF, which results from the loss of electrons precipitating into the atmosphere (Treumann, 2006, and references therein). In situ measurements performed within AKR sources by terrestrial polar orbiters such as *Viking* and *FAST* later showed that AKR waves display characteristics inconsistent with a loss cone free energy source: the radiation is primarily produced in the R-X mode perpendicularly to the magnetic field, at frequencies 1%–2% below f_{ce} and with too high flux densities. Electron measurements instead revealed that the AKR primary source of free energy resides in a shell-type EDF produced by the adiabatic motion of electrons accelerated at 1–10 kev along auroral magnetic flux tubes (Delory et al., 1998; Ergun et al., 2000; Louarn et al., 1990; Pritchett et al., 1999). The radio sources themselves are embedded within auroral density cavities colocated with layers of upward field-aligned current along magnetic flux tubes mapping to the auroral oval (Hilgers, 1992; Roux et al., 1993).

The magnetosphere of Jupiter largely differs from those of the Earth and Saturn, with a large magnetic field, Io as a prominent plasma source, auroral acceleration processes of different natures. Jupiter's rapid rotation was for instance long thought to drive the main aurorae through a field-aligned current system driven by the plasma corotation breakdown in the middle magnetosphere (Cowley & Bunce, 2001). The remote properties of Io-DAM emissions, such as a strongly oblique apparent beaming, were interpreted as the signature of loss cone driven CMI (Hess et al., 2007, 2008; Mottez & Génot, 2011; Zarka et al., 1996), while the free energy sources of the other Jovian auroral radio components remained open. The Juno spacecraft, which has been in polar orbit around Jupiter since mid-2016, aims at understanding the auroral acceleration and radio emission processes with in situ measurements (Bagenal et al., 2017).

The first results obtained by Juno challenged our view of the Jovian auroral physics. The auroral regions host three main zones: a layer of upward field-aligned current associated with the main auroral oval (called zone I, or ZI) equatorward of a layer of downward field-aligned current (called zone II or ZII) (Mauk et al., 2020). Both regions are dominated by highly energetic (50–1,000 keV) bidirectional electrons. A third region, equatorward of ZI is colocated with the Diffuse Aurora (Diff. A.). It is characterized by a peak in the 3–30 keV electron energy flux and Alfvénic fluctuations (Allegrini et al., 2020a; Gershman et al., 2019; Mauk et al., 2017). Overall, the EDFs observed in the auroral regions are prominently composed of broadband distributions rather than of monoenergetic structures (Salveter et al., 2022). The specific analysis of radio sources encountered by Juno also yielded unexpected results. The spatial distribution of DAM, HOM, and bKOM sources identified between f_{ce} and $f_{ce} + 1\%$ first revealed that they all lie along a common set of magnetic flux tubes. Also, when compared to the position of UV aurorae imaged simultaneously on 3 occasions, the radio sources map to the equatorward edge of the main UV oval (Louis et al., 2019). A growth rate analysis applied to case studies of HOM sources (near a few MHz) showed that these are driven by the CMI with a loss cone EDF as the prominent source of free energy (Louarn et al., 2017; Louis et al., 2020) and a conics EDF as a second one (Louarn et al., 2018). In a recent study, we have checked those first results with a more statistical approach (Collet et al., 2023). In a survey of the HOM source crossings observed near the 10 first perijoves, we have confirmed their systematic colocation with the polar edge of the Diff. A. zone (see also Al Saati et al., 2022). We discovered one case of HOM emission observed at $f < f_{ce}$, which we showed with an improved CMI growth rate analysis to be unambiguously driven by a shell-type EDF, as at Earth and Saturn.

In this article, we build up on this approach to exhaustively identify and analyze all the HOM sources (the most frequently encountered) observed at frequencies $f < f_{ce}$ over the first 45 perijoves, sampling the 2016–2022 interval. Section 2 describes the Juno radio, electron and magnetic data sets used. In Section 3, we review the basics of the CMI and the principles and limitations of our updated growth rate analysis. The influence of biased EDF measurements onto the calculated growth rates is assessed in Appendix A. The survey of the 15 $f < f_{ce}$ radio source crossings identified solely from radio observations is described in Section 4. We then apply in Section 5 our growth rate analysis to two representative source crossings, unraveling three different CMI-unstable, co-existing, sources of free energy. We finally discuss these results in the context of the Jovian auroral acceleration processes in Section 6.

2. Data Set

Since its arrival at Jupiter, the Juno spinning spacecraft (2 rotations per minute) has sampled its polar magnetosphere with 53 days-long (up to mid 2021, 43 days-long after), highly elliptical, orbits. Late Sept. 2022, it had completed 45 orbits, labeled by perijove (hereafter PJ). The spacecraft trajectory is such that it successively crosses the northern and southern auroral regions (before/after each PJ, hereafter referred to as PJN or PJS for simplicity) at low enough altitudes to intercept auroral magnetic flux tubes hosting auroral radio emissions. In this study, we have used observations acquired from within such radio sources by three instruments, namely the (radio and plasma) Waves experiment (Kurth et al., 2017), the JADE-E electron spectrometer (McComas et al., 2017) and the MAG flux gate magnetometer (Connerney et al., 2017), whose characteristics are briefly reminded below.

2.1. Waves

Waves measures electric fields between 50 Hz and 41 MHz with an electric dipole antenna made of two 2.8 m monopoles and two Low and High Frequency Receivers (LFR and HFR, resp.). Both receivers sample two bands: LFR-Low from 50 Hz to 20 kHz and LFR-High from 20 to 140 kHz, HFR-Low from 140 kHz to 3.5 MHz, and HFR-High from 3.5 to 41 MHz. Waves operates either in the so-called survey or burst mode. Survey observations provide time-frequency measurements, sweeping the full Waves spectral range at a cadence varying between 1 and 30 s. The 1 s cadence is used near perijoves for the sampling of auroral regions.

In this study, we focused on Burst mode HFR-Low and -High measurements between 1 and 40 MHz, covering the HOM and DAM spectral ranges. The electric field is sensed with 4096 12-bit samples at a cadence of 7 Msps (HFR-Low) and 1024 12-bit samples at a cadence of 1.3 Msps (HFR-High). These measurements can be processed by Fast-Fourier Transforms to produce high resolution 1 s × 1.709 kHz (HFR-Low) and 1 s × 1.270 kHz (HFR-High) time-frequency spectrograms. Note that in HFR-High, data are only measured in snapshots of 1 s × 1 MHz encompassing the local f_{ce} value (as measured by MAG, see below). We used these high resolution dynamic spectra to track encountered radio sources, namely emissions observed near f_{ce}, and to characterize the wave properties (frequency, duration, intensity). Whenever necessary, we estimated the physical wave flux density by cross-calibrating the burst mode spectrograms onto the survey mode observations already properly calibrated by Louis et al. (2021, 2023).

We noticed on some occasions that the radio emissions tracked throughout successive HFR-High high resolution spectrograms display a discontinuity when the central frequency of the tracked 1 MHz bandwidth changes. We suspect that, in such cases, the frequency ramp of the spectrograms is not reliable, which prevents us from confidently tracking emission below f_{ce}. The corresponding time intervals were therefore avoided in this study.

2.2. JADE-E

JADE-E is a swept-energy electron spectrometer that measures electrons at energies logarithmically spaced from 0.1 to ~100 keV. The spatial coverage was originally ensured by 3 sensors measuring the full sky EDF, out of which 1 failed during the Juno cruise phase. The EDF is measured since then by the 2 remaining sensors, with a total of 64 anodes each sampling a 7.5° field-of-view. During the auroral passes, JADE-E operates in high resolution mode, in which the EDF is measured every second. As Juno completes a rotation in 30 s, JADE-E samples all directions within this time interval. The signal is recorded successively by adjacent energy channels with a time delay of ~0.1 s. It can therefore significantly change whenever the EDF varies at sub-second timescales, producing a characteristic saw tooth profile (Louarn et al., 2018). The maximal energy sampled by JADE-E is lower when the spacecraft spin axis is not parallel to the magnetic field (down to 40 keV when the angle is about 35°).

The measured EDF can nonetheless be biased. Electron measurements are significantly depleted for pitch angles $\theta = (\mathbf{v}, \mathbf{B})$ (with **v** the electron velocity and **B** the local magnetic field) near 90° in strong magnetic field regions because of an instrumental, energy-dependent, masking of incident electrons (Allegrini et al., 2017, 2020b; McComas et al., 2017).

For our purpose, we used calibrated measurements of EDF together with values of n_e inferred from these (Louarn et al., 2017, 2018) to derive f_{pe}. Because of the missing sensor, the instrumental shadowing, and the non-sampling of electrons with energies falling outside the JADE-E range, the derived values of f_{pe} are a lower limit of the real instantaneous electron plasma frequency.

2.3. MAG

The radio/electron observations introduced above are complemented by MAG high resolution measurements of the magnetic field amplitude B and of its components. f_{ce} can thus be derived directly from the measured B, and the direction of encountered field-aligned currents (FAC) by the derivative of the azimuthal component B_ϕ (Kotsiaros et al., 2019).

3. Growth Rate Analysis

3.1. Basics of the Electron Cyclotron Maser Instability

As mentioned above, the CMI was developed to account for the terrestrial AKR (see the reviews of Treumann, 2006; Wu, 1985). It requires a tenuous and magnetized enough plasma ($f_{pe} \ll f_{ce}$) and hot, weakly relativistic, unstable electrons (of density n_h) generally embedded within a cold, prominent, electron population (of density n_c). The CMI amplifies waves near the electron gyrofrequency $\omega_{ce} = 2\pi f_{ce}$ along the resonance equation:

$$\omega = \frac{\omega_{ce}}{\Gamma} + k_\parallel v_\parallel \tag{1}$$

where $\omega = 2\pi f$ is the wave angular frequency, $\Gamma = 1/\sqrt{1 - \frac{v^2}{c^2}}$ is the Lorentz factor and $k_\parallel$ and $v_\parallel$ are the projection of the wave vector $\mathbf{k}$ and the electron velocity $\mathbf{v}$ onto the direction of the local magnetic field. In the weakly relativistic assumption, when v/c is low, $\Gamma^{-1} \approx 1 - \frac{v^2}{2c^2}$ and the resonance Equation 1 transposes into the equation of a circle in the $(v_\parallel, v_\perp)$ phase space. This resonance circle is defined by a center $(v_0, 0)$ and radius v_r such that:

$$\begin{aligned} v_0 &= \frac{k_\parallel c^2}{\omega_{ce}} \\ v_r &= c\sqrt{\frac{k_\parallel^2 c^2}{\omega_{ce}^2} - 2\left(\frac{\omega}{\omega_{ce}} - 1\right)} = \sqrt{v_0^2 - 2c^2 \Delta\omega} \end{aligned} \tag{2}$$

with $\Delta\omega = \frac{\omega - \omega_{ce}}{\omega_{ce}}$ (e.g., Galopeau et al., 2004). These two parameters determine the properties of the amplified waves: the wave number $k_\parallel$, which defines the emission angle, is directly linked to v_0, and the wave emission frequency f is linked to v_r. Equations 1 and 2 imply in particular that emission perpendicular to the magnetic field ($k_\parallel = 0$) corresponds to waves radiated at frequencies strictly below f_{ce} from resonance circles centered on $v_0 = (0, 0)$ which, as we will see, can amplify waves from shell structures present in the EDF. Conversely, oblique emission corresponds to waves radiated at frequencies slightly above f_{ce} from non-centered circles associated for instance with the loss cone part of the EDF (Hess et al., 2007).

Waves are amplified at large angles from the magnetic field, most efficiently in the Right-handed eXtraordinary (RX) mode, whenever the wave growth rate (the imaginary part of the wave angular frequency ω_i) computed from the EDF along the resonance circle is positive.

3.2. Growth Rate

The analytical expression of the growth rate results from the RX mode dispersion equation, which itself depends on the nature of the ambient plasma. Various expressions of the growth rate can be found in the literature, most of which assume that the auroral plasma is dominated by cold electrons. A general expression of the normalized growth rate $\gamma = \frac{\omega_i}{\omega_{ce}}$ can be written as:

$$\gamma = A\int_0^{\pi} d\alpha c^2 v_r^2 \sin^2(\alpha)\frac{\partial F_h}{\partial v_\perp} \tag{3}$$

where c is the speed of light, F is the EDF with the subscript h standing for the hot, and unstable, electron population, the integral is computed along the resonance circle, α is the angle formed by a radius and the $v_\parallel$ axis, and A is a coefficient whose expression varies among the authors. Wu and Lee (1979) and Wu (1985) for instance used $A = \frac{\pi^2}{4}\epsilon_h^2$, with $\epsilon_h = \frac{\omega_{ph}}{\omega_{ce}}$. A similar expression was later reused to study in situ the AKR source region (Mutel et al., 2007), the SKR one (Mutel et al., 2010), and to remotely investigate the wave properties of Jovian DAM emissions (Galopeau et al., 2004; Hess et al., 2007).

Focusing on the Jovian HOM sources, Louarn et al. (2017) introduced a new expression of the growth rate, aimed at better considering the effect of hot electrons in a prominent cold plasma, with $A = 2\pi^2\frac{\epsilon_h^2}{\epsilon_c^2}\Delta\omega^2$, where the subscript c stands for the cold thermal electron population.

In Collet et al. (2023), we derived a more general expression of the RX mode growth rate (Equation 4):

$$\gamma = \frac{\left(\frac{\pi}{2}\epsilon_h\right)^2}{1+\left(\frac{\epsilon_c}{2\Delta\omega}\right)^2}c^2\int_0^{\pi} d\alpha v_r^2 \sin^2(\alpha)\frac{\partial F_h}{\partial v_\perp}(v_0 + v_r\cos(\alpha), v_r\sin(\alpha)) \tag{4}$$

This formula simplifies to the growth rate expression of Louarn et al. (2017) (that of Mutel et al. (2010), respectively) whenever $\Delta\omega \ll \frac{\epsilon_c}{2}$ ($\Delta\omega \gg \frac{\epsilon_c}{2}$, respectively).

Overall, the growth rate is proportional to the integral of the perpendicular gradient of the hot EDF $\frac{\partial F_h}{\partial v_\perp}$ along the CMI resonance circle in the velocity space.

The CMI free energy source thus lies in the EDF portion where $\frac{\partial F_e}{\partial v_\perp}$ is positive (population inversion). Loss cone and shell structures both fulfill this condition and are thus CMI unstable. The angle of the loss cone θ_{LC} can be estimated from the expression:

$$\sin^2(\theta_{LC}) = \frac{B_o}{B_{\max}}\left(1 - \frac{e\Delta\phi}{E_o}\right) \tag{5}$$

where B_o and $E_o = \frac{m_e v^2}{2}$ are the magnetic field amplitude and energy at the observation point and $B_{\max}$ is the magnetic field amplitude for a mirror point at the boundary between the atmosphere and the magnetosphere. $\Delta\phi = \phi_o - \phi_m$ account for any electric potential difference between the atmosphere and the observation point. Whenever needed, θ_{LC} was derived by using the JRM33 internal magnetic field model (Connerney et al., 2022) combined with the most recent current sheet model (Connerney et al., 2018) assuming $\Delta\phi = 0$ and $B_{\max}$ derived at a precipitation altitude of 300 km above the 1 bar level. A variety of resonance circles can be fitted to the loss cone, corresponding to a wide range of electron energies. They generally match positive but also negative gradients, so that the associated growth rates can remain modest.

A shell structure (also referred to as a horseshoe in 2D) consists of an EDF intensification at constant velocity. It results from parallel acceleration and conservation of the first adiabatic invariant of electrons moving along field lines (Pritchett, 1984). It is highly CMI-unstable: for an idealized shell, the resonance circle fitting the inner shell boundary continuously matches positive gradients out of the loss cone, yielding high growth rates.

3.3. Search for CMI-Unstable Electrons

Electron measurements have been regularly investigated at Earth (Ergun et al., 2000; Louarn et al., 1990) and Saturn (Menietti et al., 2011; Mutel et al., 2007) to check their CMI-instability and unambiguously confirm auroral radio emission sites. This approach has been first applied to Jupiter with Juno in situ measurements by Louarn et al. (2017), who analyzed a southern HOM source crossed after PJ1.

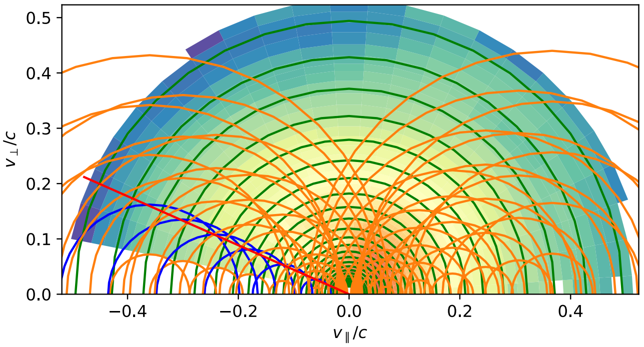

Figure 1. JADE-E measurement of an electron distribution function (EDF) displayed in the velocity space, once smoothed over three consecutive pitch angle and energy channels. The red line shows the expected loss cone aperture angle. The colored circles display a subset of centered (green) and non-centered (orange, blue) Cyclotron Maser Instability resonance circles. Only the blue circles are consistent with loss cone EDF.

Assuming a cold plasma environment, the authors derived CMI growth rates from JADE-E measurements of the EDF. The perpendicular gradient was derived from $\frac{\partial F_e}{\partial \alpha}$. This approximation is only valid for small pitch angles, thus for circles with finite centers and small radius. It was later reused by Louarn et al. (2018) and Louis et al. (2020) to study another HOM source and a higher frequency one associated with Ganymede, respectively. Overall, these authors identified both loss cone and conics-type EDF as CMI free energy sources.

As an attempt to improve this approach, we developed the following systematic method. We used the CMI growth rate expression given in Equation 4, which we computed from JADE-E data (assuming $\frac{\partial F_h}{\partial v_\perp} \approx \frac{\partial F_e}{\partial v_\perp}$) treated as follows. Each measurement of EDF was first bi-linearly interpolated over 8 adjacent pixels in both velocity (v) and pitch angle (θ) directions to achieve robust estimates of $\frac{\partial F_e}{\partial \alpha}$ and $\frac{\partial F_e}{\partial v}$.

We then tested the CMI-instability of the distribution with a total of ~4,000 resonance circles, yielding the same number of growth rates. A subset of these circles is illustrated by the example provided by Figure 1. A series of 128 circles with $v_0 = (0{,}0)$ and logarithmically distributed radii v_r ranging on the whole JADE-E energy interval (green circles), was specifically chosen to test shell-type EDF fulfilling the weakly relativistic assumption. A second series of 4,200 non-centered resonance circles, exploring the ranges $v_0 = 0.033\,c$ to $0.367\,c$ (0.28–38.3 keV) and $v_r = 0.2\,v_0$ to $1.25\,v_0$, were aimed at testing loss cone EDFs (blue circles) and any other unstable part of the EDF with $\frac{\partial F_e}{\partial v_\perp} \geq 0$ (orange circles).

More precisely, resonance circles were considered as consistent with the theoretical loss cone aperture angle θ_{LC} whenever $|\theta_{chara} - \theta_{LC}| < 7.5°$, where $\theta_{chara} = \arcsin(v_r/v_0)$ is the characteristic pitch angle of non-centered circles (see Figure 2 and Hess et al., 2008). We also define the kinetic characteristic energy of a circle as $E_{chara} = \frac{m v_{chara}^2}{2}$ with $v_{chara} = \sqrt{|v_0^2 - v_r^2|}$ for non centered circles and $v_{chara} = v_r$ for centered circles. E_{chara} corresponds to the energy of the hot electron population where the resonance circle is tangent to the loss cone, where the wave amplification is in principle maximal.

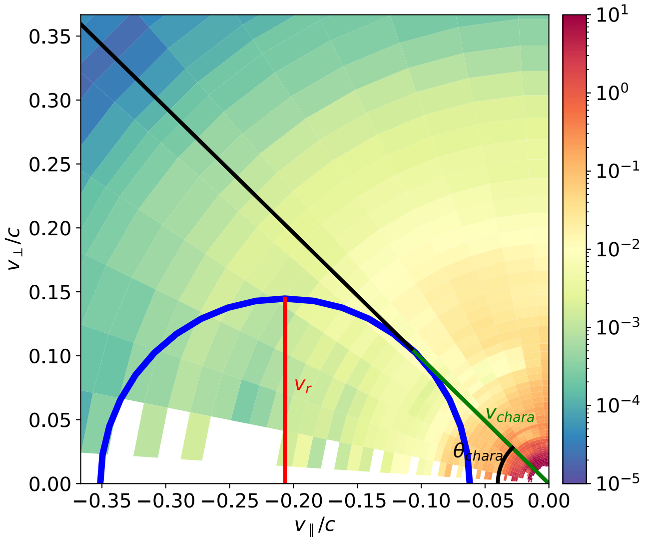

Figure 2. Same as Figure 1 with a single resonance circle defined by its coordinates v_0 and v_r yielding the characteristic electron speed v_{chara} (green line) and angle θ_{chara} (black angle). The tested circle is consistent with a loss cone type electron distribution function whenever $|\theta_{chara} - \theta_{LC}| < 7.5°$.

Resonance circles intercepting less than 20 ($v_\parallel$, $v_\perp$) data points or more than 13% unphysical data points with $F_e \leq 0$ (resulting from background subtraction and low SNR) were not considered. Also, to deal with sub-second variations of instrumental origin producing a saw tooth profile able to erroneously yield positive growth rates for centered circles, we additionally imposed the condition that centered resonance circles must yield positive growth rates for at least two consecutive circles in radius/energy.

3.4. Wave Intensity

From the growth rate, we can derive the expected spectral flux density S in W m^{-2} Hz^{-1} and compare it to the one measured by Waves. S can be expressed as $S = G\,S_0$ with S_0 the amplitude of source radio waves and G the gain factor associated with the wave growth. The expression of G can be written as:

$$G = \exp\left(\frac{4\pi f_{ce} \gamma L_c}{v_g}\right) \tag{6}$$

where L_c is the convective length and v_g is the RX mode wave group velocity (Mutel et al., 2010).

For the sake of simplicity, we chose a constant group velocity $v_g = 0.1\ c$, as derived for the auroral region of Saturn by Mutel et al. (2010). A more precise

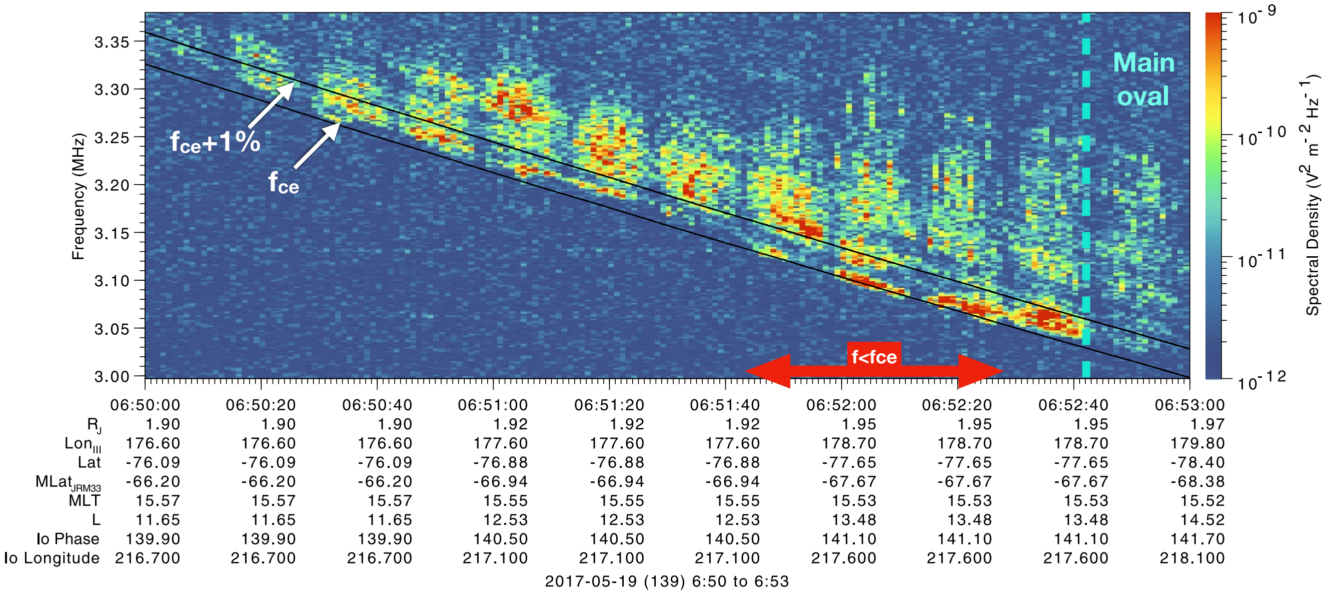

Figure 3. High resolution time-frequency spectrogram during the southern auroral pass following PJ6. The two black solid lines plot f_{ce} and f_{ce}+1%. HectOMetric emissions are observed near 3 MHz below f_{ce} + 1% over the full 3 min-long interval and strictly below f_{ce} from 06:51:45 to 06:52:27 UT. Both radio sources are colocated with the Diff. A. zone, equatorward of the main UV auroral oval (Collet et al., 2023).

estimate of v_g would require to solve the dispersion relation with a relativistic analytical model of the EDF - such as delta ring or DGH distributions (Pritchett, 1984; Wu, 1985)—in the observed Jovian hot and highly depleted auroral plasma environment, which is beyond the scope of this paper.

We use the galactic background radio spectrum as a source term, $S_0 \sim 10^{-19}$ W m^{-2} Hz^{-1} for frequencies of a few MHz (Dulk et al., 2001). We note that an alternate source term could be the incoherent noise from hot electrons (Zarka et al., 1986).

This growth rate analysis will be illustrated on two representative cases of encountered radio sources in Section 5.

4. Survey of $f < f_{ce}$ Radio Emissions

A straightforward approach to identify radio sources encountered along the Juno trajectory is to search for emissions observed at frequencies near f_{ce} by Waves. Louis et al. (2019) led a survey of bKOM, HOM, and DAM sources over the 15 first perijoves by tracking emission between f_{ce} and $f_{ce} + 1\%$, an empirical detection criterion chosen from the early results of Louarn et al. (2017). This ad hoc criterion is not unambiguous though, as emission $f > f_{ce}$ can correspond to either a really crossed source or a nearly distant one since the CMI emission frequency depends on the velocity of resonant electrons.

In a recent re-analysis of candidate radio sources observed over the first 10 perijoves with high resolution Waves observations, we unexpectedly identified several cases of HOM and DAM emission at frequencies strictly below f_{ce} reminiscent of the AKR and SKR sources observed in situ at Earth and Saturn (Collet et al., 2023). Interestingly, $f < f_{ce}$ emission can only be driven by the CMI from shell-type EDF, which had not been reported at Jupiter to date. The case of the southern HOM source observed during PJ6S and studied in detail in (Collet et al., 2023) is illustrated in the Waves time-frequency spectrogram of Figure 3.

In this follow-up study, we extend our survey to perijove 45, covering a 6 years-long time interval ranging from mid-2016 to Sept. 2022, to achieve an exhaustive list of $f < f_{ce}$ candidate radio sources. Out of these, we identified 13 events with $f < f_{ce}$ between 1 and 3 MHz in the HFR-Low band and 2 events between 4 and 5 MHz in the HFR-High band, resulting in a total of 15 candidate sources with $f < f_{ce}$, all corresponding to the HOM range. Table 1 lists these candidate sources together with their properties. We rejected 8 ambiguous cases of $f < f_{ce}$ emissions observed by HFR-High.

Table 1

Catalog of $f < f_{ce}$ HectOMetric Emissions Identified From Waves Observations Over PJ1-45

PJ	Interval	f (MHz)	$\frac{f-f_{ce}}{f_{ce}}$	$\frac{f_{pe}}{f_{ce}}$	UV aurorae	Mono energetic signature	$\frac{n_h}{n}$	FAC direction	Alfvén waves	Shell energy (keV)	Enlargement of LC	Normalized growth rate (x10^{-4})	Size (10^3 km)	Estimated intensity (W. m^{-2}.Hz^{-1})
1S	2016-08-27 13:29:29-30:51	5	−0.6%	4×10^{-3}	Poleward.		0.5	↑	X	0.2	X	0.3–0.8	0.25	7.9×10^{-10}
6S	2017-05-19 06:51:45-52:27	3	−0.2%	10^{-3}	Diffuse	X	0.8	↑		0.5–3	X	0.2–2	2	8.02×10^{-12}
11N	2018-02-07 12:57:24-36	2.5	−0.3%	2×10^{-3}	Main Oval		0.8	↑	X	1	X	0.5–1	0.6	1.85×10^{-11}
11S	2018-02-07 14:44:54-45:19	2.8	−0.25%	3×10^{-3}	Main Oval		0.8	↑	X	2	X	0.5–3	1.25	2.56×10^{-11}
21N	2019-07-21 03:08:05-29	2.6	−0.25%	2×10^{-3}	Diffuse	X	0.7	↓		3	X	0.2–2	1.2	1.20×10^{-11}
24S	2019-12-26 19:04:04-54	1	−0.3%	3×10^{-3}	Diffuse	X	0.15	↑		1	X	0.2–0.8	2,5	2.69×10^{-11}
25S	2020-02-17 19:11:43-57	1.2	−0.2%	3×10^{-3}	Poleward		0.5	↑		0.2–0.7	X	2–3	0.75	4.13×10^{-11}
28S	2020-07-25 07:14:06-51	2.2	−0.3%	2×10^{-3}	Main Oval	X	0.5	↑		2	X	0.5	2	4.00×10^{-12}
31S	2020-12-30 23:08:24-09:20	1.1	−0.25%	2×10^{-3}	Main Oval	X	0.6	↑↓		2–3	X	0.3–3	2.5	8.27×10^{-12}
32S	2021-02-21 18:42:13-43	2.2	−0.55%	10^{-3}	Diffuse	X	0.7	↑	X	1.5	X	0.1–1	0.8	1.5×10^{-11}
35N	2021-07-21 7:27:30-40	4.0	−0.2%	2×10^{-3}	Diffuse		0.7	*	*	0.2	X	0.5	1–10	6×10^{-10}
37S	2021-10-16 18:22:33-25:39	1.6	−0.4%	3×10^{-3}	Main Oval		0.4	↓		3	X	2–20	(1+) 3	1.29×10^{-11}
38S	2021-11-29 15:34:35-36:34	1.1	−0.4%	2×10^{-3}	Diffuse		0.5	↑		4	X	1–20	(0.5+) 1.5	8.27×10^{-12}
41S	2022-04-09	1.3	−0.3%	5×10^{-3}	Diffuse		0.6	↑		5	X	2–10	2.75	3.50×10^{-11}

Table 1
Continued

PJ	Interval	f (MHz)	$\frac{f-f_{ce}}{f_{ce}}$	$\frac{f_{pe}}{f_{ce}}$	UV aurorae	Mono energetic signature	$\frac{n_h}{n}$	FAC direction	Alfvén waves	Shell energy (keV)	Enlargement of LC	Normalized growth rate (x10^{-4})	Size (10^3 km)	Estimated intensity (W. m^{-2}.Hz^{-1})
	17:05:40-06:35													
44S	2022-08-17 16:17:14-34	0.9	−0.8%	4×10^{-3}	Diffuse	X	0.5	↑		5	X	0.2–1	1.0	2.69×10^{-10}

Note. Columns 1 and 2 indicate the perijove and the event time interval. Columns 3, 4, and 5 give the absolute and relative emission frequency at the point where the emissions are the lowest below f_{ce}, together with the $\frac{\omega_{pe}}{\omega_{ce}}$ ratio. Column 6 indicates whether Juno was magnetically colocated with the main auroral oval or with the Diff. A. zone located from UVS images, column 7 whether the JADE-E spectrum exhibited a mono-energetic signature, column 10 whether we identified Alfvenic perturbations from MAG measurements, and column 9 the upward/downward sense of FAC (not identified on PJ35N). Column 8 indicates the ratio of hot to total electron density. Columns 12–14 provide the radio wave properties derived from our CMI growth rate analysis and the source size along the spacecraft trajectory. The last column gives the source peak spectral flux density as observed by Waves.

For comparison purposes, we also compiled a list of $f_{ce} < f < f_{ce} + 1\%$ candidates radio sources, provided in supplementary material (Collet et al., 2024), which includes both HOM and DAM emissions.

The modest but significant number of $f < f_{ce}$ HOM events provides the opportunity to assess their average spatial distribution. First of all, out of the 15 events, only 3 were observed in the northern hemisphere and 12 in the southern one. Their footprints are plotted (green symbols) together with those of $f_{ce} < f < f_{ce} + 1\%$ events (orange symbols) in the southern polar projections of Figure 4, on top of the Juno footpath with M-Shell between ~$70R_J$ and ~$5R_J$ (gray lines). The northern (Figures 4a1 and 4b1) and southern (Figures 4a2 and 4b2) polar projections are displayed in planetocentric coordinates (Figures 4a1 and 4a2) and as a function of magnetic latitude and magnetic Local Time (MLT, Figures 4b1 and 4b2). The magnetic footprints of field lines mapping to 15 and 60 R_J (1 R_J = 71,492 km = a Jovian radius) at the magnetic equator are indicated by the blue dashed lines and taken as boundaries of the main auroral oval.

Overall, the $f < f_{ce}$ HOM emissions are not homogeneously distributed, as opposed to the $f_{ce} < f < f_{ce} + 1\%$ HOM/DAM ones. Altogether, the former are roughly distributed at all MLTs, except in the 11–16 sector. Nonetheless, we note that 9 events out of 15 (60%) are confined in the 02–11 MLT dawn side. Looking at longitudes, the emission regions all lie between 80° and 270°, with the exception of a single one observed near 330°. The $f < f_{ce}$ radio sources are located along flux tubes with M-shells between 17 and 50 R_J, consistent with the average location of the main auroral oval. We compare the relative locus of radio and UV auroral emissions in more detail in Section 5.3.

5. Multi-Instrumental Analysis of $f < f_{ce}$ Radio Sources

To unambiguously validate and characterize the $f < f_{ce}$ HOM source candidates listed in Table 1, we study all cases with Juno multi-instrumental observations and our CMI growth rate analysis described in Section 3.3 and show below two representative southern cases.

5.1. The Case of PJ32S

5.1.1. Radio Source and Auroral Context

The case of PJ32S stands as a typical illustration of $f < f_{ce}$ southern HOM sources. Figure 5 provides a summary of radio and particle measurements observed between 18:40:00 to 18:45:00 UT on day 2021-02-21. Figure 5a shows a high resolution radio dynamic spectrum ranging from 1.9 to 2.4 MHz. We observe emissions between f_{ce} and f_{ce} + 1% from 18:40:10 to 18:43:45 UT (black dashed rectangle) and emissions strictly below f_{ce}, down to f_{ce} − 0.5%, from 18:42:30 to 18:43:00 UT (red dashed rectangle).

Figure 5b shows the electron plasma frequency f_{pe} (left-handed y-axis) derived from JADE-E measurements of the total electron density n_e (right-handed y-axis) with black crosses. The contribution of energetic electrons n_h

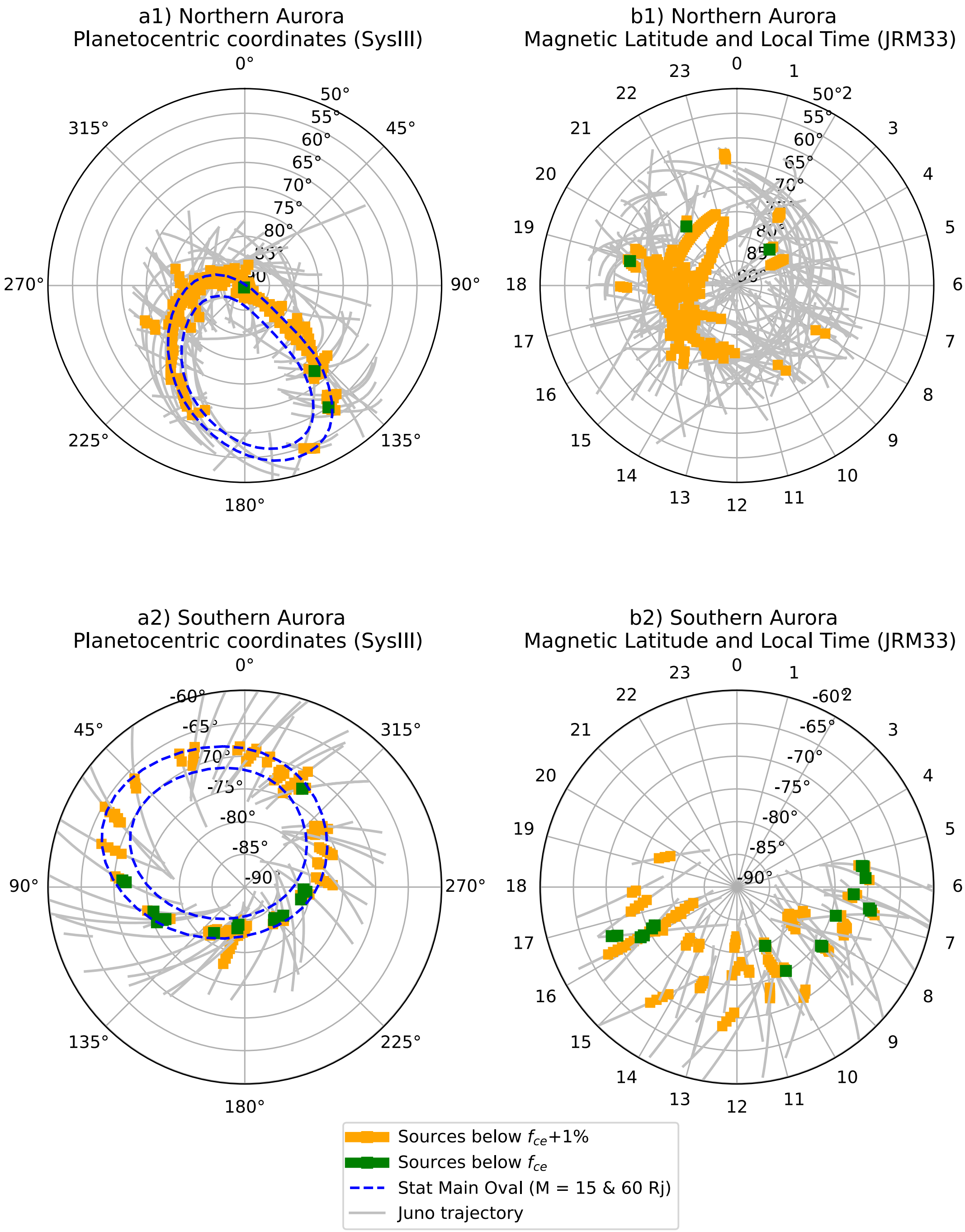

Figure 4. (a_1, b_1) Northern and (a_2, b_2) southern magnetic polar projections displayed in (a_1, a_2) planetocentric SIII coordinates and (b_1, b_2) as a function of the magnetic latitude and the magnetic local time. The Juno footpath (gray lines), together with the magnetic footprints of $f_{ce} < f < f_{ce} + 1\%$ (orange symbols) and $f < f_{ce}$ (green symbols) radio emission regions, have been derived from magnetic projection based on the Juno JRM33 and current sheet model (Connerney et al., 2020, 2022) at 300 km altitude above the 1-bar level (Gustin et al., 2016). The inner and outer blue dashed lines indicate field lines with magnetic apex (M-shell) located at 15 and 60 R_J, respectively.

(we assume their density is the one from electrons with energy above 1 keV) is displayed by red crosses. The solid lines plot the upper envelope of both series of symbols to remove unphysical drops resulting from instrumental shadowing/spacecraft spin. Overall, f_{pe} is sharply decreasing between 18:42:00 and 18:43:00 from 10 kHz ($n_e \sim 1.5$ cm^{-3}) to 2 kHz ($n_e \sim 0.05$ cm^{-3}) resulting in f_{pe}/f_{ce} ratios as low as 1×10^{-3}. Energetic electrons become prominent after 18:42:00 with $n_h \sim 0.7 n_e$.

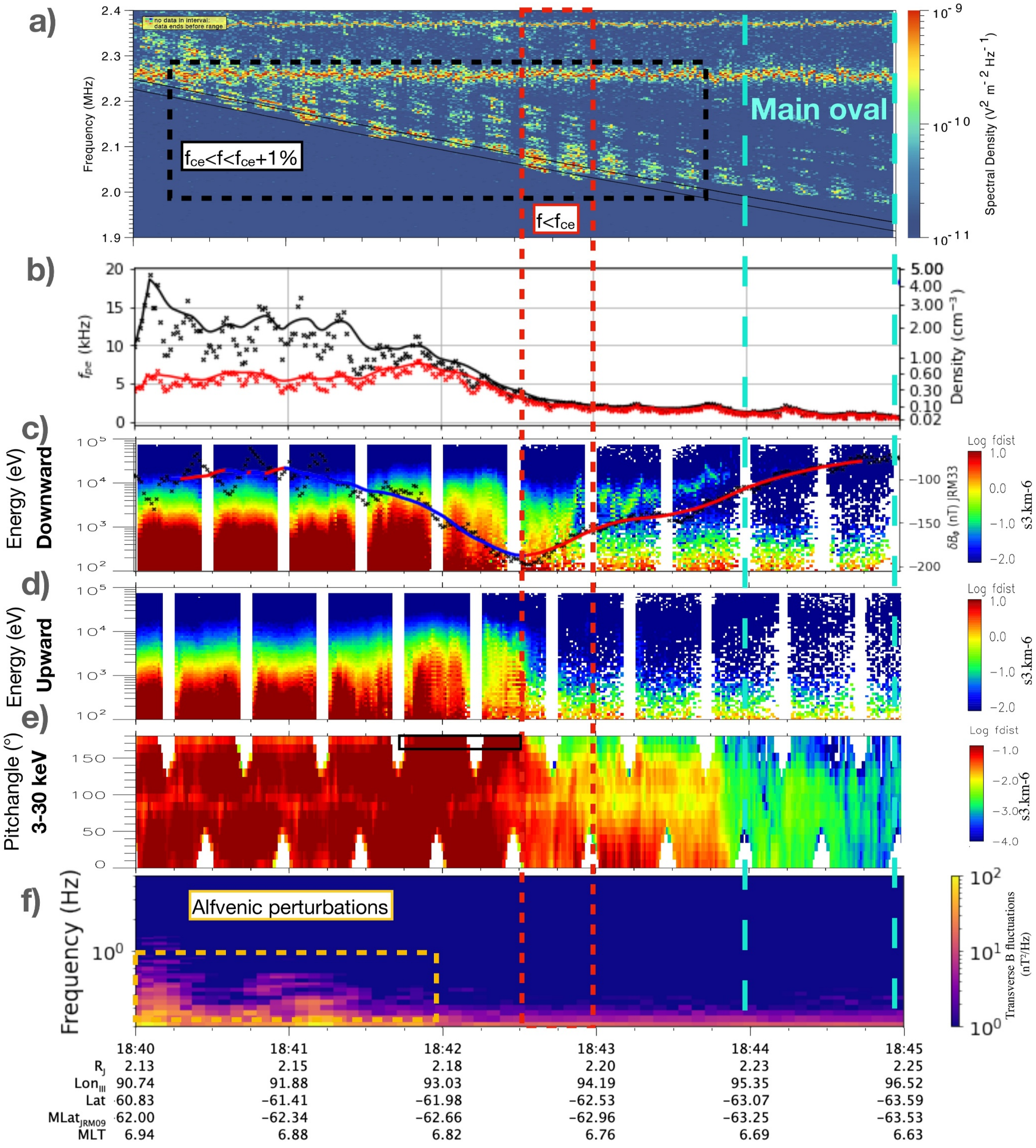

Figure 5. Juno radio and particle measurements obtained during PJ32S on day 2021-02-21. (a) Waves high resolution time-frequency spectrogram. The two solid black lines plot f_{ce} and $f_{ce} + 1\%$. The dashed red (black, resp.) boxes indicate emission at frequencies $f < f_{ce}$ ($f < f_{ce} + 1\%$, resp.). The vertical blue dashed line marks the timing after which Juno was colocated with the main UV auroral oval. The horizontal signal seen near 2.27 MHz is an instrumental radio frequency interference. (b) Electron plasma frequency f_{pe} (left-handed y-axis) or electron plasma density n_e (right-handed y-axis) plotted as a function of time, as derived from JADE-E for all electrons (black crosses) and for those above 1 keV only (red crosses). The solid lines plot the upper envelope of the density. (c) Time-energy spectrogram of the downward electron flux ($\theta < 30°$). The azimuthal magnetic field is superimposed on the panel with the right-handed y-axis. Its blue and red portions indicate downward and upward field-aligned currents. (d) Same as (c) for the upward electron flux ($\theta > 150°$). (e) Time-pitch angle spectrogram of the electron flux integrated between 3 and 30 keV. (f) Time-frequency spectrogram of the transverse perturbations of the magnetic field. The yellow box indicates Alfvénic fluctuations (during which no compressive perturbations were observed, supporting their Alfvénic nature).

Figures 5c and 5d show time-energy electron spectrograms in the downward ($\theta < 30°$) and upward ($\theta > 150°$) direction, respectively, while Figure 5e displays the time pitch-angle spectrogram for 3–30 keV electrons. On top of Figure 5c is superimposed the azimuthal magnetic field, whose blue and red portions indicate downward and upward FAC. Clear signatures of downward monoenergetic electrons between 1 and 20 keV form inverted Versus observed between 18:42:45 to 18:44:15, overlapping both the upward FAC layer starting equatorward of the main UV oval and the $f < f_{ce}$ HOM emission. The density of this monoenergetic population (unseen for upgoing electrons) is decreasing with increasing energy. Figure 5f shows a time-frequency spectrogram of transverse magnetic field fluctuations (as defined in Gershman et al. (2019) as the spectrogram of the normalized trace of the power spectral matrix). Alfvénic fluctuations are visible equatorward of the main oval, from 18:40:00 to 18:42:00 (orange dashed rectangle), reminiscent of those identified by Gershman et al. (2019).

From the above results, we can infer the position of the auroral zones. Alfvénic fluctuations are characteristic of the Diff. A. region. However, since their amplitude is known to decrease with increasing 3–30 keV electron flux (hereafter 18:41:30), the Diff. A. region plausibly ends between 18:42:00 and 18:42:30. The $f < f_{ce}$ HOM emission lies strictly equatorward of the main UV auroral oval while coinciding with a depletion of the total electron density and with the upward FAC layer consistent with region ZI.

5.1.2. Growth Rate Analysis

Figure 6 illustrates our growth rate analysis on the example of the EDF sampled by JADE-E at 18:42:46 UT, chosen middle in the $f < f_{ce}$ HOM emission region. Figure 6a shows the EDF in the velocity plane, with the red line indicating the loss cone aperture θ_{LC}. The plotted resonance circles are those maximizing the growth rate for the shell (green), loss cone (blue), and ”other” (orange, neither shell nor loss cone) categories. Figure 6b replicates Figure 6a while plotting $\frac{\partial F_e}{\partial v_\perp}$ instead of F_e. The blue circle indeed intercepts gradients close to the theoretical loss cone whereas the orange circle intercepts gradients at pitch angles slightly larger than $\theta_{LC} + 7.5°$ ($\sim 10°$). The green circle is tangent to a partial shell best visible for downgoing electrons and peaking near $v \sim 2.10^7$ m s^{-1} $= 0.06\ c$ (1.1 keV).

Figures 6c and 6d plot all the calculated growth rates as a function of (v_0, v_r) and as a function of $\Delta\omega$. In Figure 6c, the black lines delimit the area of resonant circles consistent with the loss cone aperture. The associated growth rates are displayed by blue dots in Figure 6d. The shell and other resonance circles are displayed with green diamonds and orange crosses (sub-dividing into “X” for circles associated with upward electrons and “+” for downward ones), respectively. The maximal growth rate for each of the 3 categories of circles is marked by a symbol in Figure 6c and by its associated resonance circle in Figures 6a and 6b.

Overall, two portions of the investigated EDF yield $\frac{\partial F_e}{\partial v_\perp} > 0$ and are therefore simultaneously CMI-unstable. The maximal growth rate $\gamma = 5.4 \times 10^{-5}$ is obtained for the shell-centered resonance circle associated with a weakly energetic electron horseshoe feature at 0.9 keV and expected emission frequency slightly below f_{ce}. The loss cone and other categories yield lower maximal growth rates of 1.2 and 1.1 $\times$ 10^{-6}, respectively, associated with electrons of 5.3 and 4.6 keV characteristic energies and expected emission near $f_{ce} + 1\%$.

Figure 5a displays distinct radio emissions both below and above f_{ce} consistent with predictions, thus supporting simultaneous CMI wave amplification by both parts of the EDF. The comparison between the observed and predicted spectral flux densities is addressed at the end of this Section.

5.1.3. Sources of Free Energy

Figure 7 shows the results of our growth rate analysis applied to the full time interval of Figure 5. Figure 7a displays the maximal growth rate for each category of resonance circle as a function of time. Figure 7b plots the associated characteristic electron energy. Figure 7c shows a high resolution radio dynamic spectrum, here plotted as a function of $\Delta\omega = (f - f_{ce})/f_{ce}$, on top of which are plotted the emission frequencies derived from the radius of resonance circles yielding large enough growth rates (we arbitrarily chose the condition $\gamma > 10^{-5}$, found below to be a good compromise).

The 3 categories of circles simultaneously display positive growth rates, with γ ranging from 10^{-7} to a few 10^{-4}, over the whole interval, thus extending the results of the example EDF presented above. Before 18:42:20, the loss cone growth rates (blues dots) are prominent, gradually rising from 10^{-7} to 10^{-4}. They correspond to 0.3–30 keV

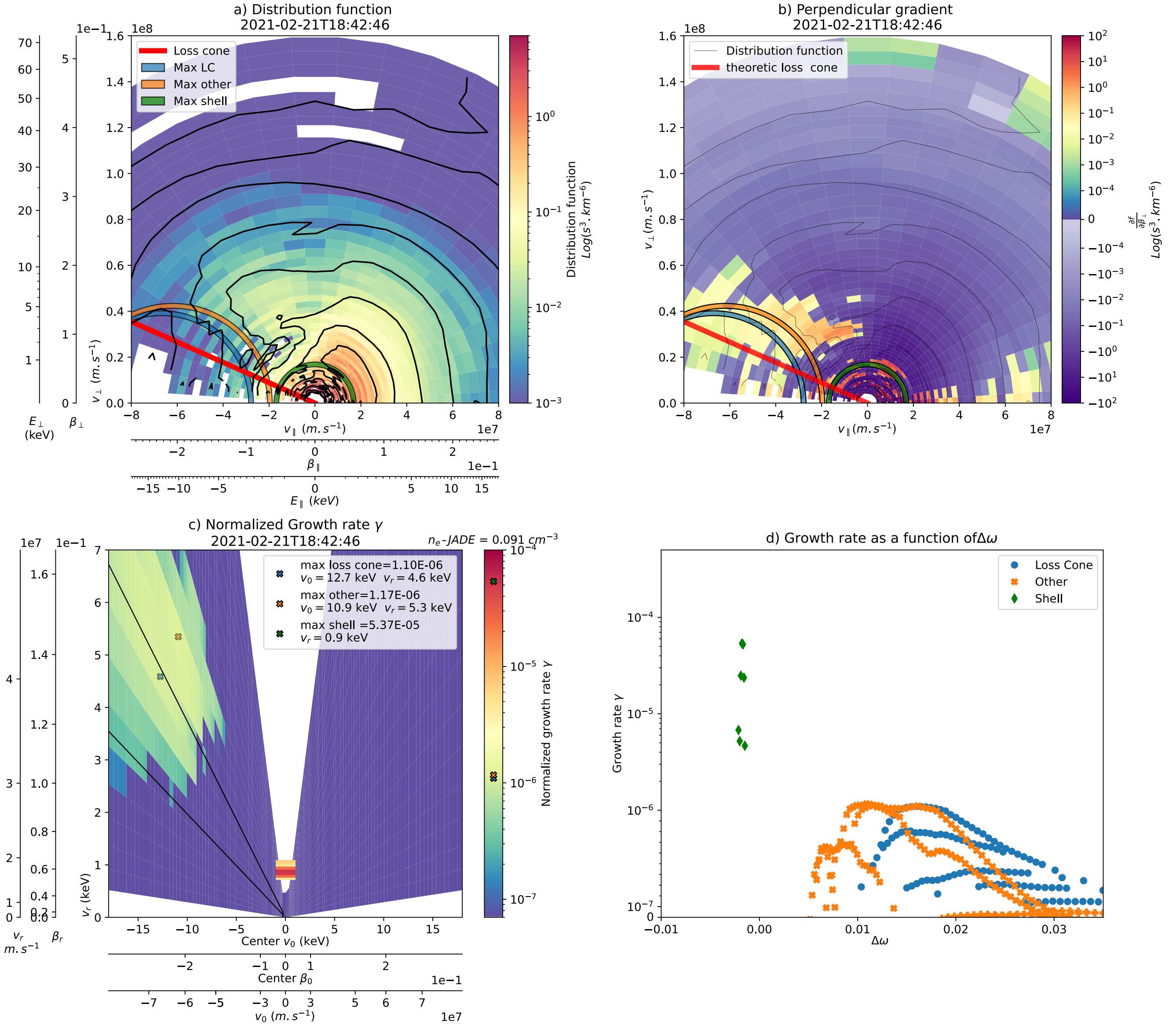

Figure 6. Cyclotron Maser Instability (CMI) growth rate analysis of the electron distribution function (EDF) measured by JADE-E on 2021-02-21 18:42:46 UT (PJ32S). (a) EDF displayed in the $(v_\parallel, v_\perp)$ phase space. For the sake of clarity, each axis displays velocities v in m/s, relative velocities $\beta = \frac{v}{c}$, and associated energies $E = \frac{1}{2}m_e v^2$ in keV. The black lines map isocontours of the EDF smoothed over 3 consecutive energy and pitch angle channels. The red line plots the theoretical loss cone aperture angle. The green, blue, and orange circles correspond to those yielding the maximal growth rates for the categories of CMI resonance circles testing shell-type, loss cone-type, and other (neither shell nor loss cone) unstable electrons. (b) Same as (a) with $\frac{\partial F_e}{\partial v_\perp}$ plotted instead of F_e. (c) CMI growth rate displayed as a function of the center v_0 and the radius v_r. The 2 black lines enclose the area corresponding to loss cone-type resonance circles. (d) CMI growth rate displayed as a function of $\left(\Delta\omega = \frac{1}{2c^2}\left(v_0^2 - v_r^2\right)\right)$. The green, blue, and orange symbols again correspond to shells, loss cones, and other types of resonance circles. For the latter category, the "+" and "x" symbols distinguish between circles intercepting positive $\frac{\partial F_e}{\partial v_\perp}$ for electrons propagating downward or upward, respectively. For this time interval, the largest growth rates were obtained for upward electrons, such as for the loss cone resonance circles.

electrons and emission frequencies of a few 0.1% above f_{ce} consistent with the HOM low frequency envelope observed below $f_{ce} + 1\%$. We note at this occasion that the cone emission angle ranges from 92° to 96° for the most unstable loss cone circles.

Positive shell growth rates (green diamonds) appear after 18:42:10, peaking at a few 10^{-4} before monotonically decreasing down to 10^{-6} at 18:45:00. They correspond to electron energies increasing from 0.2 to 26 keV, and emission frequencies below f_{ce}. The latter matches the $f < f_{ce}$ HOM low frequency cutoff observed down to $f_{ce} - 0.5\%$ between 18:42 and 18:43 (for 1–3 keV electrons). Within this interval, electron energies vary similarly

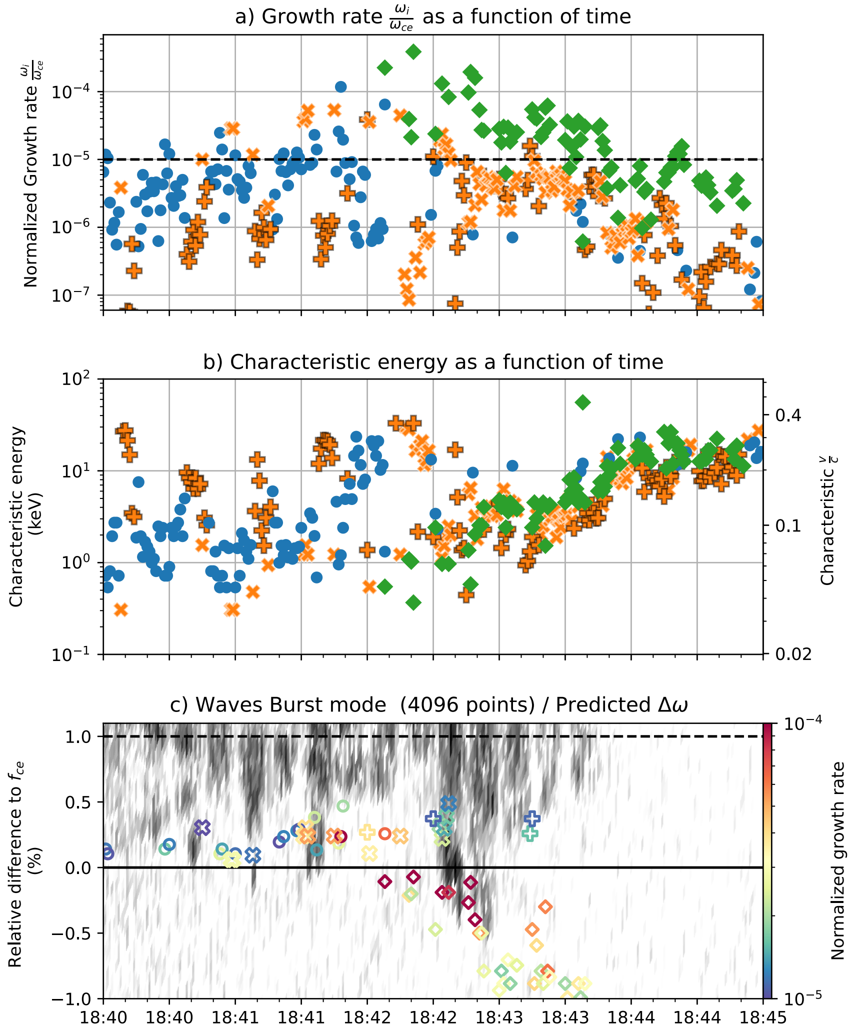

Figure 7. Cyclotron Maser Instability growth rate analysis applied to the full-time interval of Figure 5. (a) Maximum growth rate as a function of time for each electron distribution function measurement (1-s cadence) for the shell (green diamonds), loss cone (blue circle), upward other (orange "x" crosses), and downward other (orange "+" crosses) types of resonance circles. (b) Associated electron characteristic energy as a function of time. (c) Waves high resolution dynamic spectrum plotted as a function of time and frequency relative to f_{ce}. The colored symbols map the predicted wave emission frequency for positive growth rates $\geq 10^{-5}$.

to the inverted Versus identified in Figure 5c, with energy increasing with time. After 18:43:00, shell growth rates predict radio emission below $f_{ce} - 0.5\%$ which is unobserved by Waves.

We now focus on the third type of resonance circles. Figure 8 displays the characteristic aperture of both the other and loss cone circles with crosses and dots, respectively, for upgoing (top, $v_{\|} < 0$) and downgoing (bottom, $v_{\|} > 0$) portions of the EDF. As reminded above, the circles associated with upgoing electrons were classified as loss cone whenever $|\theta_{chara} - \theta_{LC}| < 7.5°$, lying within the two black dashed lines on Figure 8a. This condition left circles consistent with an enlarged loss cone, well visible between 18:42:30 and 18:43:50. This enlargement might probe a downward acceleration experienced by the EDF consistent with the upward FAC layer encountered during this interval and/or a downward potential drop located below the spacecraft. These circles generate emissions between 92° and 98° to the direction of the magnetic field. Figure 8b also reveals a significant amount of other circles associated with the downgoing portion of the EDF, where $\frac{\partial F_e}{\partial v_\perp} > 0$ (well visible on the right-hand side of Figure 6b). The population inversion probed by those circles is reminiscent of the conics-type EDF identified by Louarn et al. (2018). These circles generally yielded modest growth rates, corresponding to expected emission near $f_{ce} + 0.2 - 0.3\%$ with emission angles from 84° to 86°, for instance, observed at 18:42:30 and 18:43:20.

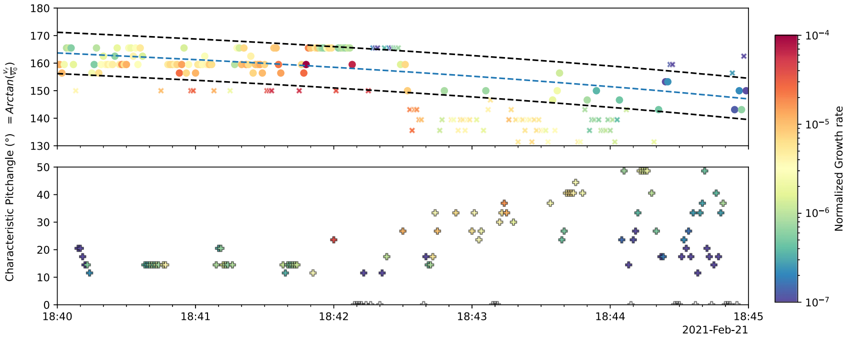

Figure 8. Characteristic pitch angle $\theta_{chara} = \arcsin(v_r/v_0)$ of the loss cone-type (filled circle) and other-type (crosses) resonance circles yielding the maximum growth rate displayed in Figure 7a as a function of time for (top) up going and (bottom) downgoing electrons. The blue dashed line on the top panel indicates the theoretical loss cone aperture angle, and the black lines its ±7.5° uncertainty. Loss cone (other) resonance circles therefore lie within (outside) these black lines. The blue-to-red color scale corresponds to increasing growth rates.

The non-observation of radio waves expected to be amplified below $f_{ce} + 0.5\%$ from 18:41:40 and 18:42:30 and below $f_{ce} - 0.5\%$ after 18:43:00 from 2 to 20 keV electrons may be explained by transient, smaller sized, sources resulting in lower wave spectral flux densities, below the Waves' sensitivity threshold. From 18:42:00 to 18:42:30, the loss cone was generally filled in (black rectangle in Figure 5e), and unstable loss cone EDFs were not detected continuously.

Overall, our growth rate analysis validated shell-type EDF as the CMI free energy source for $f < f_{ce}$ HOM emissions, in addition to the already known prominent loss cone EDF being responsible for HOM emission observed between f_{ce} and $f_{ce} + 0.5\%$. HOM emission observed between $f_{ce} + 0.5\%$ and $f_{ce} + 1\%$ in turn most likely corresponded to a slightly distant (uncrossed) emission region.

5.1.4. Wave Intensity

As described above, the wave spectral flux density can be derived from the growth rate, along with Equation 6, assuming $v_g = 0.1\ c$.

The convective length can be derived from the overall time interval τ_{cross} during which $f < f_{ce}$, which yields 1,000 km. We then transpose this source length along the spacecraft trajectory to its equivalent latitudinal extent as a more realistic estimate, so that $L_c \approx 350$ km.

We then derive a gain $G \approx 10^{27}$. This tremendous value is unrealistic and may result from either an overestimated convective length, or an underestimated group velocity, or a combination of both.

The former possibility can be explored by a refined analysis of the crossed sources. Section 5.1.2 pointed out that unstable shell-type electrons at energies consistent with the observed emissions last for about 8 s. This reduced time interval corresponds to a latitudinal extent of ≈100 km. This yields a more realistic gain $G = 10^9$, which in turn provides a theoretical wave intensity of $S = 10^{-10}$ W m^{-2} Hz^{-1} which well compares to the observed $S_{Waves} = 10^{-11}$ W m^{-2} Hz^{-1}.

Suppose we alternately consider the $L_c = 350$ km value as reliable and use the observed wave intensity as a reference observable to infer v_g. By inverting Equation 6, we obtain a necessary gain of $G = 10^8$, requiring $v_g = 0.34\ c$.

The respective role of these two free parameters is discussed in more details in Section 6.

5.2. The Case of PJ28S

Hereafter, we similarly investigate a second representative case of a $f < f_{ce}$ HOM event observed on day 2020-07-25 during PJ28S.

5.2.1. Radio Source and Auroral Context

Figure 9 provides the auroral context between 07:12:00 and 07:15:30 UT in a format identical to Figure 9. HOM emissions at $f < f_{ce}$ ($f < f_{ce} + 1\%$, resp.) are visible in Figure 9a between 07:14:05 and 07:14:50 (between 07:13:30 and 07:15:05, resp.). The $f < f_{ce}$ HOM emission region coincides with a prominent hot plasma in Figure 9b and with inverted-V shaped mono-energetic downward electron beams, visible in Figure 9c, labeled A (from 07:14:30 to 07:15:00) followed by a second interval labeled B (from 07:15:00 to 07:15:30). The latter does not coincide with $f < fce$ emissions. Similarly, weaker, signatures are simultaneously visible for upgoing electrons in Figure 9d, suggesting bidirectional acceleration. Upward and downward FAC signatures alternate during the interval, the $f < f_{ce}$ event overlapping with the upward FAC layer visible between 07:13:51 and 07:15:00. Figure 9e provides the JADE-E pitch angle coverage for 3–30 keV electrons and additionally shows that the loss cone (indicated by the horizontal line) was sporadically filled in (black rectangles). Alfvénic fluctuations characteristic of the Diff. A. are clearly visible from 07:12:10 to 07:14:15, overlapping the first half of the $f_{ce} < f < f_{ce} + 1\%$ HOM emission region. The locus of the main UV auroral oval during this interval was unclear. However, we notice upward FAC from 07:13:45 to 07:14:45. We then infer that the Diff. A. spans the time interval associated with Alfvénic fluctuations from 07:12:15 to 07:14:10 and ZI from 07:14:10 to 07:14:45. The emissions below f_{ce} were thus detected mostly in ZI.

5.2.2. Growth Rate Analysis and Sources of Free Energy

Figure 10 displays the results of our growth rate analysis in a format identical to Figure 7. In Figure 10a, the three types of circles again yield positive growth rates between $\sim 10^{-7}$ and $\sim 10^{-4}$.

The most intense ones are obtained for shell EDFs associated with electrons of 0.5–2 keV (Figure 10b) consistent with both monoenergetic electron signatures A and B observed in Figure 9c. Figure 10c illustrates the excellent correspondence between the predicted and observed wave emission frequencies below f_{ce} for event A only.

Throughout the interval, we observe modest growth rates associated with the loss cone resonance circles. These maximize at the middle of the interval with $\gamma \sim 10^{-5}$. The expected emissions near $f_{ce} + 0.1\%$, corresponding to weakly energetic electrons ≤ 1 keV, were generally not observed. We note some episodes during which the loss cone is filled in and other ones during which JADE-E did not sample upward electrons, though.

Other circles associated with both downgoing and upgoing electrons are observed. The latter again displays a slightly larger aperture than the loss cone circles, indicating here again a loss cone enlargement (and the same emission angles range as PJ32S). They coincide with the monoenergetic structures with maximal growth rates $\sim 5 \times 10^{-5}$ during event B. The expected emission near $f_{ce} + 0.15\%$, associated with electrons of ~ 2 keV, is observed. The rest of other circles associated with downward electrons display growth rates as modest as the loss cone ones, peaking at $\sim 10^{-5}$ at the start of event A. The predicted emission near $f_{ce} + 0.1$–0.2%, with electrons ranging from 0.4 to 2 keV, corresponds to the most intense HOM emission observed throughout the interval.

5.2.3. Wave Intensity

Computing the wave intensity requires a precise estimation of γ. In this case, EDFs used for calculation were significantly affected by shadowing near $\theta \sim 90°$, thus biasing the growth rate toward a lower value. We show in Appendix A that this instrumental bias can be corrected by multiplying shell growth rates by a correcting factor, here estimated to be 1.85.

Similarly to PJ32S, we can compute from the source crossing a source size of 2,500 km along the spacecraft path which is equivalent to a latitudinal extent $L_c = 1{,}100$ km. Using $v_g = 0.1\ c$ and $\gamma \sim 9 \times 10^{-5}$, we obtained a gain $G = 10^{40}$.

Once again, this value is tremendous compared to the observed emission intensity of $4 \times 10^{-12}\ \mathrm{W\ m^{-2}\ Hz^{-1}}$.

We have found that, together with $f < f_{ce}$ radio emissions, unstable shell-type EDFs are detected for only 7 s. This corresponds to a latitudinal convective length $L_c \approx 200$ km which in turn results in $G \approx 10^{7.4}$ and $S = 2 \times 10^{-12}$. This source size seems then to be consistent with the observations.

Conversely, since there is a factor of 5 between the exponents of the gain deduced from JADE-E and the one deduced from Waves, we could also deduce an adjustment in the group velocity to $v_g = 0.5\ c$.

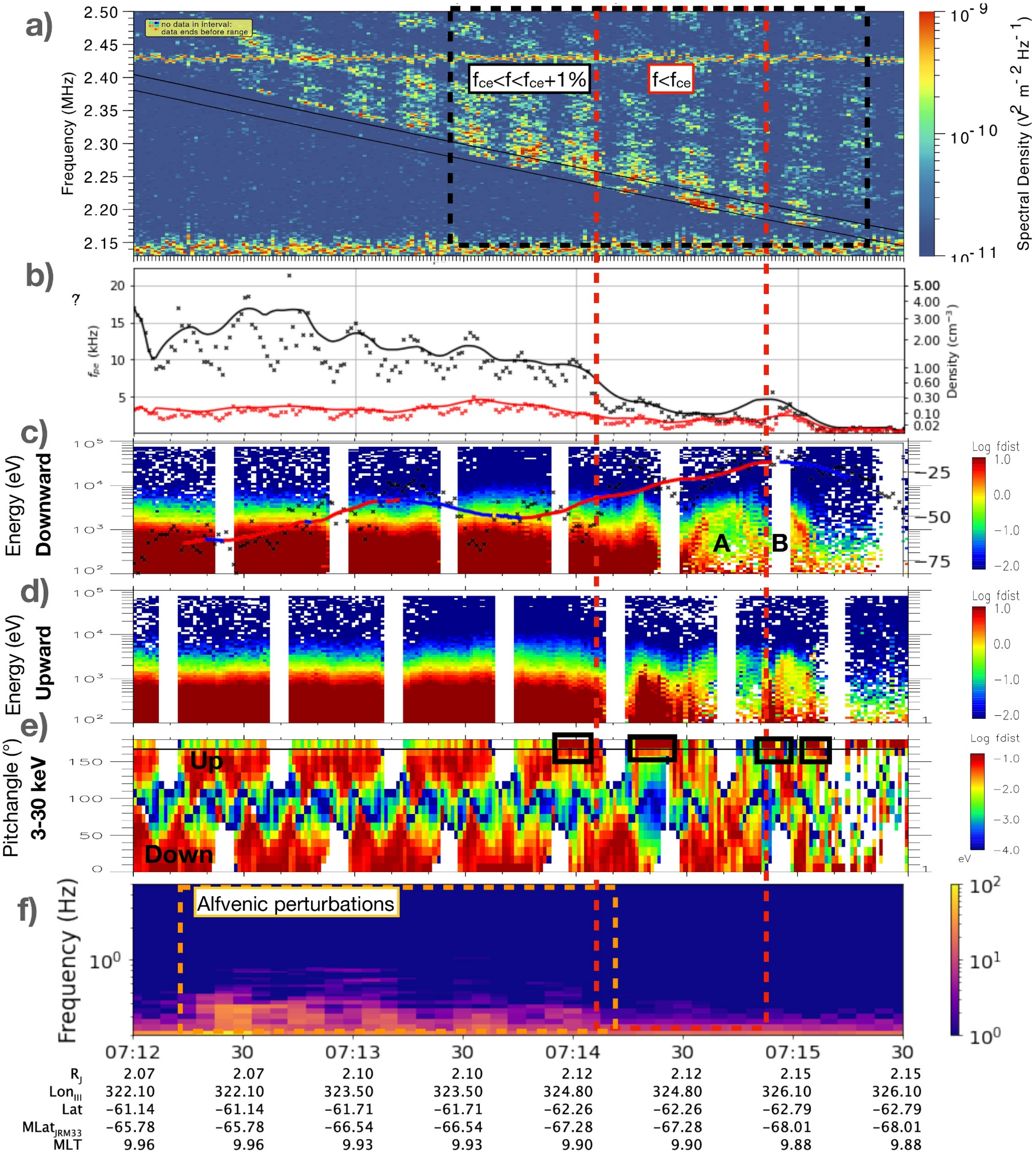

Figure 9. Same as Figure 5 for PJ28S.

5.3. Statistical Study

To achieve a more comprehensive view of the $f < f_{ce}$ HOM sources, we applied our growth rate analysis to all the events from our survey, frequencies ranging from 1 to 3 MHz, whose characteristics are listed in Table 1.

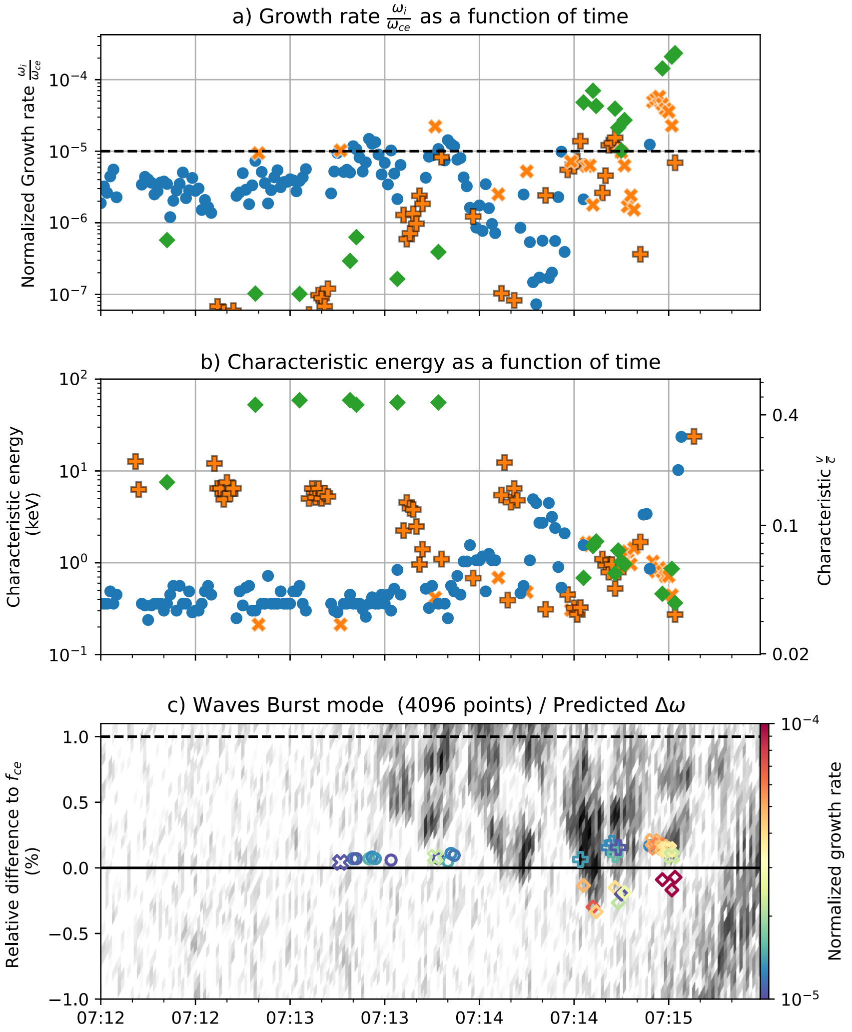

Figure 10. Same as Figure 7 for PJ28S.

We have identified CMI-unstable shell EDF for all of these events, with predicted emission properties in excellent agreement with those simultaneously observed below f_{ce}. This validates shell EDF as a new, third, CMI source of free energy driving HOM emission at Jupiter and the robustness of the $f < f_{ce}$ criterion to unambiguously track in situ crossed radio sources. Coincident signatures of monoenergetic electron structures were seen on JADE-E spectra in 7 cases.

The plasma region hosting the $f < f_{ce}$ HOM sources is hot and tenuous with $n_h/n_{tot} \sim 0.6$ and $\frac{\omega_{pe}}{\omega_{ce}} \sim 2 \times 10^{-3}$ on average. The radio sources were hosted along flux tubes with magnetic apex (M-shell) ranging from 17 to 50 R_J. The magnetic footprints of 8 sources are colocated with the diffuse UV auroral emissions, 5 with the main oval and 2 poleward of it. As opposed to the case study of (Collet et al., 2023), only 4 sources coincide with Alfvénic fluctuations. 12 sources lie within an upward FAC layer and match a gradual electron depletion. According to the criteria proposed in Mauk et al. (2020); Sulaiman et al. (2022), the sources are located near the boundary between Diff. A. and ZI (a definite identification of which would have required the analysis of highly energetic electrons sampled by Juno/JEDI, which we did not include in this study). We only found obvious monoenergetic structures in JADE-E energy spectra for 7 events.

The most unstable shell resonance circles correspond to growth rates up to a few 10^{-4} associated with weakly energetic electrons of 0.2–5 keV. The observed wave spectral flux densities S_{obs} range from 4×10^{-12} to 7.9×10^{-10} W m^{-2} Hz^{-1}. The latter, largest, value (observed at 5 MHz during PJ1S) transposes to

4.0×10^{-20} W m^{-2} Hz^{-1} at 1 astronomical unit, slightly below the median (50% occurrence level) intensity derived from statistical Waves observations (Louis et al., 2021). In other words, the crossed HOM sources corresponded to weak emissions, as observed remotely on average by Waves.

Poleward of the $f < f_{ce}$ detected sources, we regularly identified CMI-unstable shell EDF with large growth rates associated with more energetic, 2–20 keV, electron beams but, surprisingly, without any visible radio counterpart. We have also identified at some occasions unstable shell resonance circles at larger (up to 30 keV) energies, unrelated to the $f < f_{ce}$ observed HOM sources, yielding growth rates $\gamma \lesssim 10^{-6}$, likely too low to amplify radio waves above the Waves sensitivity threshold.

Loss cone and other CMI-unstable EDFs are always present during the $f < f_{ce} + 1\%$ source crossings and encompass the $f < f_{ce}$ ones. We noticed a systematic enlargement of the loss cone similar to the one discussed in the two above case studies.

6. Discussion

The statistical identification of previously unreported shell-driven CMI Jovian HOM emissions reminiscent of AKR at Earth and SKR at Saturn provides a new basis for comparative discussion.

The $f < f_{ce}$ HOM source region corresponds to a hot, highly depleted, plasma with $\frac{\omega_{pe}}{\omega_{ce}} \sim 10^{-3}$, 1 order of magnitude less than at Earth and Saturn. As for Saturn, such values are low enough to drive the CMI whenever any type of unstable EDFs are present, and the radio sources were not coinciding with Earth-like cavities characterized by sudden drops of the total electron density.

The normalized growth rates derived in this study range from 0.2 to 20×10^{-4} whatever the free energy source. These values are typically 1 order of magnitude less than those previously published at Jupiter (Louarn et al., 2017; Louis et al., 2020), which we attribute to our different expressions of the CMI growth rate.

The large contribution of hot electrons to the total density challenges the cold plasma approximation. Determining growth rates in a hot plasma requires the use of numerical methods (Pritchett, 1984; Pritchett et al., 1999;, and references therein) or to analytically derive the dispersion relation by assuming a specific hot plasma population (Wong et al., 1982). Such complex calculations are beyond the scope of this study.

The vast majority of $f < f_{ce}$ HOM sources coincide with upward current layers, like AKR and SKR, but they were generally located along flux tubes equatorward of the main auroral oval which stands as a major difference with the terrestrial and kronian cases. The poor matching between the position of the main oval and upward FAC or the sporadic unexpected coincidence between the main oval and Alfvenic fluctuations renders the identification of auroral zone I and the region of diffuse aurora ambiguous. However, there is no obvious reason that these regions do not overlap.

Our survey of $f < f_{ce}$ HOM sources revealed a strong north/south asymmetry with only 3 unambiguous sources detected in the north. The northern auroral region proved to host more complex and dynamical FAC systems (Al Saati et al., 2022) which may result in less frequent and/or more transient electron beams producing shell EDF than in the southern auroral region.

The source electrons of the $f < f_{ce}$ observed HOM sources display lower energies, typically within 0.2–5 keV, than at Earth (1–10 keV) and Saturn (1–20 keV). The associated emission frequencies are therefore close to f_{ce} (0.2–0.8% to be compared to 1–2% for AKR/SKR). Indeed, according to Equation 1, for shell-driven CMI, the larger the electron energy, the lower the emission frequency. Weakly energetic electrons of a few keV were to be expected, as the CMI equation transposes into a resonance circle in the velocity space in the weakly relativistic assumption. Nonetheless, it is interesting to note that more energetic (5–50 keV) CMI-unstable shell EDF with large growth rates were systematically detected poleward of the tracked $f < f_{ce}$ sources, but without any radio counterpart. Smaller sources might be a plausible reason for preventing wave amplification beyond the Waves' sensitivity threshold. The increase in energy of the shell EDF toward the pole was correlated with a decrease in the total electron density, as expected from a static current system (Knight, 1973).

The detected shell EDF results from the adiabatic evolution along auroral flux tubes of mono-energetic electrons beams, which are much less frequently observed than broadband distributions along high latitude flux tubes (Salveter et al., 2022). The reason why no radio emission is detected along flux tubes mapping to the main auroral oval and populated by highly energetic electrons of several hundreds of keV (Gérard et al., 2019), together with the validity of the CMI in strongly relativistic conditions, is left for future studies.

The wave intensity values derived for the two perijoves studied above strongly depend on the chosen group velocity and convective length. v_g has been considered to be equal to the speed of light in recent studies on DAM and HOM as a first approximation (Louarn et al., 2017, 2018; Louis et al., 2021). We chose instead the $v_g = 0.1\ c$ value derived in the cold plasma approximation for the SKR source region by Mutel et al. (2010). The results presented in Sections 5.1.4 and 5.2.3 suggest that v_g might be larger. A definite answer requires to solve the dispersion relation for the hot and low $\frac{f_{pe}}{f_{ce}}$ Jovian hectometric source region. Recently, Ning et al. (2023) updated the results of Mutel et al. (2010) for Saturn by solving the dispersion relation by taking into account the relativistic effect of the hot population. Unexpectedly, the authors found that the emissions driven by shell-type EDF should be produced on an unstable trapped mode (named R1 in their study). Assuming that HOM electromagnetic waves are trapped, their escape from the source region as RX free-space mode waves would remain to be explained. We point out here that this specific R1 mode was already theoretically derived by Le Queau and Louarn (1989) from a parametrical analysis of the X mode dispersion relation using DGH functions. These authors identified the different regimes of X mode CMI and showed in particular that this specific mode connects to the usual escaping X mode when hot electrons dominate and that the cold electron component is negligible whenever $\frac{n_{cold}}{n_{hot}}\tau^2 < 3/5$ (with τ the ratio of the thermal speed of hot electrons to that of cold ones). They also showed that the $\frac{f_{pe}}{f_{ce}}$ ratio plays a crucial role in the determination of the wave propagation conditions. The low values observed in the Jovian auroral region therefore appear as a key parameter to consider.

Similarly, the source convective length was here first estimated from the latitudinal extent of the overall source identified with Waves as a realistic source size, as opposed to the expression $L_c = \tau_{cross} v_{Juno}$ used by Louarn et al. (2017). We then refined the value of L_c by considering the effective duration for unstable JADE-E data matching the source region, which turned out to be ~3 times lower. The effective median duration of all $f < f_{ce}$ HOM/DAM sources reaches ~300 km. This is only slightly larger than the typical 100 km length of individual AKR sources (Hilgers et al., 1991) and compares to the size of SKR sources of a few 100 km, also found to be filamented (Lamy et al., 2018).

To derive the expected wave intensity, we supposed that the emission is not saturated. We can check this assumption from the AKR study of Pritchett (1984), who estimated a saturation time of about 50 ω_{pe}^{-1} in the case of 5 keV shell-type EDF with $\frac{\omega_{pe}}{\omega_{ce}} = 0.05$. Assuming that the 50 times lower $\frac{\omega_{pe}}{\omega_{ce}}$ ratio observed in the HOM source region would not significantly change this expression, we obtain a mean theoretical saturation time of ~3 ms at Jupiter. Here, with a median convective length of 300 km, and assuming a group velocity $v_g = 0.3\ c$, we obtain a typical wave interaction time of 4 ms. This result either shows that in the particular case of $f < f_{ce}$ HOM, saturation is an important aspect of the intensity computation or that the source size is overestimated.

Apart from shell EDF responsible for $f < f_{ce}$ emission, we noticed the presence of other CMI-unstable circles probing upgoing electrons near the loss cone or downgoing ones over time periods longer than the $f < f_{ce}$ studied sources and consistent with wave emission observed slightly above f_{ce}. During the $f < f_{ce}$ sources, different portions of the same EDF could therefore amplify radio emission below and above f_{ce} simultaneously. The systematic enlargement of the loss cone likely results from downward electron acceleration consistent with upward FACs and/or kinetic Alfvén waves. These phenomena are also known to be able to generate shell-type EDFs (Hess et al., 2007). We then hypothesize that this enlargement of the loss cone and the shell feature are generated by the same structures.

The maximal frequency reached by $f < f_{ce}$ HOM sources of our survey was about 5 MHz. The reason why we did not detect DAM sources beyond 5 MHz likely relates to the altitude at which the auroral flux tubes were crossed, favoring the HOM range. Still, the Jovian auroral radio spectrum peaks in the hectometric range, and HOM/DAM sources are spatially colocated, so that the studied HOM sources can be taken as representative of both HOM/DAM components. As the mission progresses the northern altitudes sampled decrease while the southern ones increase.

7. Summary and Conclusions

In this work, we have surveyed Juno/Waves high resolution observations acquired near Juno perijoves from PJ1 to PJ45, covering the time period from mid-2016 to late 2022, to identify all the radio sources within 1–40 MHz observed strictly below f_{ce}. We detected 15 such sources between 1 and 5 MHz corresponding to HOM emissions only, at frequencies 0.2%–0.8% below f_{ce}. A vast majority of these were sampled in the southern hemisphere, located along flux tubes mapping to 17–50 R_J and clustered within 80–270° longitude.

We have then analyzed these sources with an improved CMI growth rate analysis based on EDF in situ measurements by JADE-E. This analysis confirmed the CMI as a generation mechanism and a shell-type EDF involving weakly energetic electrons of 0.2–5 keV as the source of free energy of $f < f_{ce}$ HOM emissions. This statistically confirms and extends the discovery and analysis of a HOM source with $f < f_{ce}$ by (Collet et al., 2023).

The Jovian $f < f_{ce}$ HOM sources exhibit similarities and differences with the AKR observed at Earth and the SKR at Saturn.

As at Earth and Saturn, the sources are located in a hot and depleted plasma ($\frac{\omega_{pe}}{\omega_{ce}} \sim 2 \times 10^{-3}$ on Jupiter, 6×10^{-2} at Saturn (Mutel et al., 2010) and 0.1 at Earth), coinciding with upward FAC, and displaying a typical size of ~300 km. The shell electrons correspond to inverted-V monoenergetic structures.

As opposed to the terrestrial case, the emission region does not coincide with large-scale auroral cavities. Contrary to the AKR/SKR cases, $f < f_{ce}$ HOM sources are generally not connected with the main auroral oval. They are driven by slightly less energetic electron beams (~0.2–5 keV) and lead to CMI growth rates as large as a few 10^{-4}. More energetic (5–50 keV) shell EDFs were systematically observed poleward but without any detected radio counterpart.

Other CMI-unstable EDF, such as loss cone or conics ones, previously identified as primary sources of free energy for HOM sources, were also systematically observed to produce high enough growth rates to drive HOM emissions between f_{ce} and $f_{ce} + 5\%$, so that different portions of the same EDF can be simultaneously CMI-unstable and amplify waves below and above f_{ce}. The loss cone aperture was found to be systematically larger than expected, indicating the presence of auroral potential structures leading to additional acceleration of electrons into the ionosphere.

A pending important question concerns the eventual generation of radio waves by the prominent highly energetic electrons of a few 100 keV found above the auroral oval (Allegrini et al., 2020b). Clues for such a CMI amplification have yet to be identified whether below or above f_{ce} (Collet et al., 2023). This analysis will require the analysis of Juno/JEDI electron measurements. The growth analysis method developed in this study also aims to be extended to the study of bKOM sources at lower frequencies/larger altitudes. Beyond Jupiter, this approach could also be redeployed for the re-analysis of auroral radio sources crossed at Earth by various polar orbiters, at Saturn by Cassini, and soon at Mercury by Bepi-Colombo.

Appendix A: Influence of Biased EDF Onto the Calculated Growth Rate

In this Section, we investigate the influence of instrumental shadowing of JADE-E EDF measurements at pitch angles near 90° (McComas et al., 2017) on the determination of shell-driven CMI growth rates. Figure A1a shows the EDF measured on 2020-07-25 at 07:14:45, once smoothed over 3 consecutive energy and pitch angles channels, and corresponding to the PJ28S case dealt with in Section 5.2. The green circle indicates the centered resonance circle yielding the maximal growth rate, fitting a partial shell structure. The shadowing is well visible for anodes sampling pitch angles between 52.5° and 97.5° with low values of F_e.

To fill in the biased region (considered as a data gap), we suppose that the shell was isotropic and we populated the 52.5–97.5° region (between red lines) with the median value of EDF measured between $\theta = 97.5°$ and $\theta = 135°$. We chose to only take into account the downward part of this shell distribution as it would be difficult to estimate, for the upward part of it, to what extent the shell structure has propagated and where it is interrupted by the loss cone. This corrected distribution is shown in Figure A1b. Figure A1c compares the maximal growth rates obtained for the original distribution (in blue) and for the corrected one (in orange). We observe here that in contrast to the originally obtained growth rates, the corrected curve displays 2 local maxima: the first one is close to the

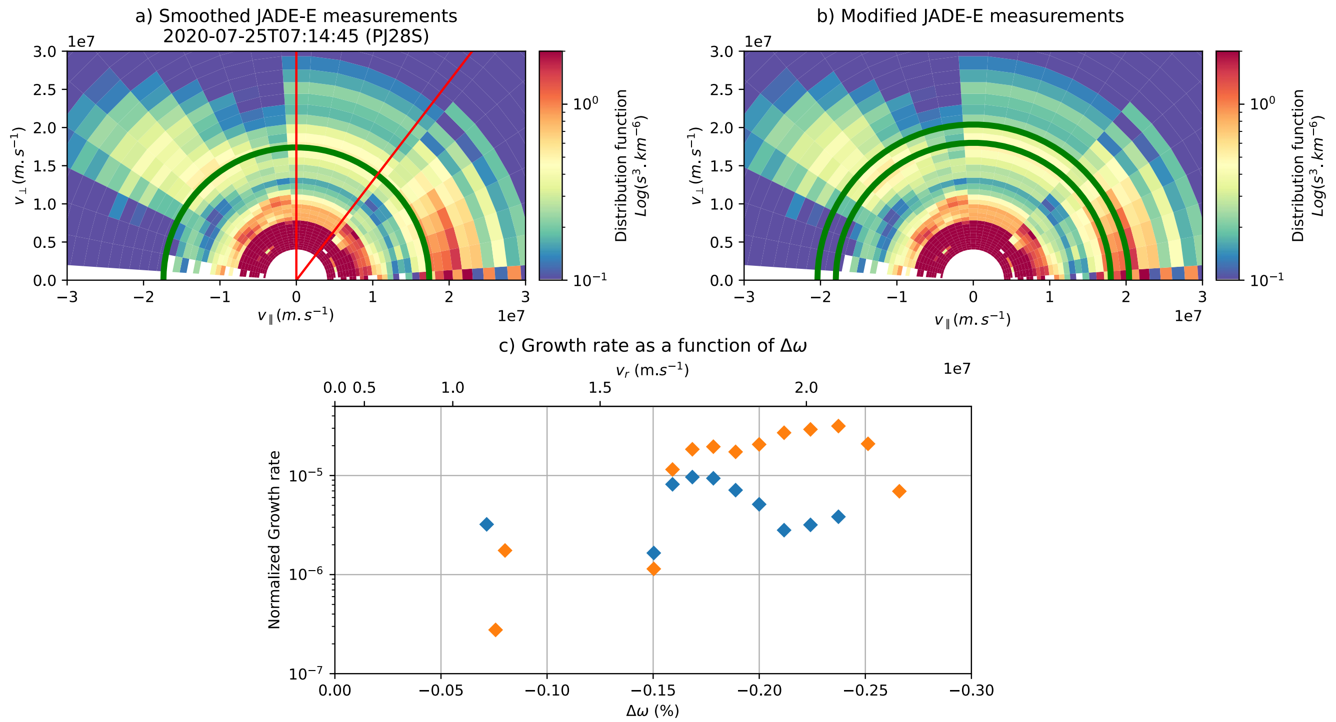

Figure A1. Original (a) and corrected (b) JADE-E electron distribution function measurement on 2020-07-25 07:14:45 (PJ28S). (c) Growth rates computed for both distributions.

original maximum while the second one is at slightly higher energy (0.068 *c*/1.18 keV instead of 0.058 *c*/860 eV). This difference in energy results in an emission frequency change of less than 0.1%.

We note here that this second peak could either be related to the shadowing itself impacting more on this part of the gradient or that it could be due to variation below the 1s time resolution of JADE E, causing a sawtooth profile. From the growth rate corresponding to these peaks, we estimate that the factor between the maximum growth rate affected by the shadow and the corrected growth rate is between 1.85 and 4.8. While this interval is quite large for a correction factor, it gives us a better estimate of the growth rate estimation than using the biased JADE-E data. Further work is needed to overcome this shadowing, one could work on a statistical study of this shadowing impact or use simulations to reproduce the shadowing as Allegrini et al. (2017) did. Such a precise study is beyond the scope of this work.

Data Availability Statement

The Juno data used in this manuscript are reachable from the Planetary Data System at https://doi.org/10.17189/1522461 (Kurth, 2021) for Waves data, at https://doi.org/10.17189/1519715 (Wilson, 2020) for JADE-E data and at https://doi.org/10.17189/1519711 (Connerney, 2017) for MAG data. The Juno/Waves estimated flux density Collection (Version 02) (Louis et al., 2021, 2023) is available at https://doi.org/10.25935/fwtq-v202. Figure 4 was produced using a list of HOM/DAM source crossings in Supplementary Information (Collet et al., 2024).

Acknowledgments

The French authors acknowledge support from CNES and CNRS/INSU national programs of planetology (PNP) and heliophysics (PNST, also funded by CEA). B. Collet thanks E. Penou at IRAP, for his help with the particle analysis through the CLWeb software, B. Bonfond for providing a useful catalog of UVS auroral images which provided the auroral context for some interpretation discussed in this paper, and the LESIA laboratory for allowing access to its internal servers.

References

Allegrini, F., Bagenal, F., Bolton, S., Connerney, J., Clark, G., Ebert, R. W., et al. (2017). Electron beams and loss cones in the auroral regions of Jupiter. *Geophysical Research Letters*, *44*(14), 7131–7139. https://doi.org/10.1002/2017GL073180

Allegrini, F., Mauk, B., Clark, G., Gladstone, G. R., Hue, V., Kurth, W. S., et al. (2020a). Energy flux and characteristic energy of electrons over Jupiter's main auroral emission. *Journal of Geophysical Research: Space Physics*, *125*(4), e2019JA027693. https://doi.org/10.1029/2019JA027693

Allegrini, F., Mauk, B., Clark, G., Gladstone, G. R., Hue, V., Kurth, W. S., et al. (2020b). Energy flux and characteristic energy of electrons over Jupiter's main auroral emission. *Journal of Geophysical Research: Space Physics*, *125*(4), e2019JA027693. https://doi.org/10.1029/2019ja027693

Al Saati, S., Clément, N., Louis, C. K., Blanc, M., Wang, Y., André, N., et al. (2022). Magnetosphere-ionosphere-thermosphere coupling study at Jupiter based on Juno's first 30 orbits and modeling tools. *Journal of Geophysical Research: Space Physics*, *127*(10), e2022JA030586. https://doi.org/10.1029/2022JA030586

Bagenal, F., Adriani, A., Allegrini, F., Bolton, S., Bonfond, B., Bunce, E., et al. (2017). Magnetospheric science objectives of the Juno mission. *Space Science Reviews*, *213*(1–4), 219–287. https://doi.org/10.1007/s11214-014-0036-8

Collet, B., Lamy, L., Louis, C., Zarka, P., Prangé, R., Louarn, P., et al. (2024). List of hom/dam radio sources crossings during Juno's 45 first perijoves [dataset]. *Zenodo*. https://doi.org/10.5281/ZENODO.10869372

Collet, B., Lamy, L., Louis, C. K., Zarka, P., Prangé, P., Louarn, P., et al. (2023). Characterization of Jovian hectometric sources with Juno: Statistical position and generation by shell-type electrons. In C. K. Louis, C. M. Jackman, G. Fischer, A. H. Sulaiman, & P. Zucca (Eds.), *Planetary, solar and heliospheric radio emissions ix*. DIAS and TCD. https://doi.org/10.25546/103095

Connerney, J. (2017). Juno j fluxgate magnetometer calibrated data v1.0 [dataset]. *NASA Planetary Data System*. https://doi.org/10.17189/1519711

Connerney, J. E. P., Benn, M., Bjarno, J. B., Denver, T., Espley, J., Jorgensen, J. L., et al. (2017). The Juno magnetic field investigation. *Space Science Reviews*, *213*(1), 39–138. https://doi.org/10.1007/s11214-017-0334-z

Connerney, J. E. P., Kotsiaros, S., Oliversen, R. J., Espley, J. R., Joergensen, J. L., Joergensen, P. S., et al. (2018). A new model of Jupiter's magnetic field from Juno's first nine orbits. *Geophysical Research Letters*, *45*(6), 2590–2596. https://doi.org/10.1002/2018GL077312

Connerney, J. E. P., Timmins, S., Herceg, M., & Joergensen, J. L. (2020). A Jovian magnetodisc model for the Juno era. *Journal of Geophysical Research: Space Physics*, *125*(10). https://doi.org/10.1029/2020ja028138

Connerney, J. E. P., Timmins, S., Oliversen, R. J., Espley, J. R., Joergensen, J. L., Kotsiaros, S., et al. (2022). A new model of Jupiter's magnetic field at the completion of Juno's prime mission. *Journal of Geophysical Research: Planets*, *127*(2), e2021JE007055. https://doi.org/10.1029/2021JE007055

Cowley, S., & Bunce, E. (2001). Origin of the main auroral oval in Jupiter's coupled magnetosphere–ionosphere system. *Planetary and Space Science*, *49*(10–11), 1067–1088. https://doi.org/10.1016/s0032-0633(00)00167-7

Delory, G., Ergun, R., Carlson, C., Muschietti, L., Chaston, C., Peria, W., et al. (1998). Fast observations of electron distributions within AKR source regions. *Geophysical Research Letters*, *25*(12), 2069–2072. https://doi.org/10.1029/98gl00705

Dulk, G. A., Erickson, W. C., Manning, R., & Bougeret, J.-L. (2001). Calibration of low-frequency radio telescopes using the galactic background radiation. *Astronomy & Astrophysics*, *365*(2), 294–300. https://doi.org/10.1051/0004-6361:20000006

Ergun, R. E., Carlson, C. W., McFadden, J. P., Mozer, F. S., & Strangeway, R. J. (2000). Parallel electric fields in discrete arcs. *Geophysical Research Letters*, *27*(24), 4053–4056. https://doi.org/10.1029/2000GL003819

Galopeau, P. H. M., Boudjada, M. Y., & Rucker, H. O. (2004). Evidence of Jovian active longitude: 1. Efficiency of cyclotron maser instability. *Journal of Geophysical Research*, *109*(A12). https://doi.org/10.1029/2004JA010459

Gérard, J.-C., Bonfond, B., Mauk, B. H., Gladstone, G. R., Yao, Z. H., Greathouse, T. K., et al. (2019). Contemporaneous observations of Jovian energetic auroral electrons and ultraviolet emissions by the Juno spacecraft. *Journal of Geophysical Research: Space Physics*, *124*(11), 8298–8317. https://doi.org/10.1029/2019JA026862

Gershman, D. J., Connerney, J. E. P., Kotsiaros, S., DiBraccio, G. A., Martos, Y. M., Viñas, A. F., et al. (2019). Alfvénic fluctuations associated with Jupiter's auroral emissions. *Geophysical Research Letters*, *46*(13), 7157–7165. https://doi.org/10.1029/2019GL082951

Gustin, J., Grodent, D., Ray, L., Bonfond, B., Bunce, E., Nichols, J., & Ozak, N. (2016). Characteristics of north Jovian aurora from STIS FUV spectral images. *Icarus*, *268*, 215–241. https://doi.org/10.1016/j.icarus.2015.12.048

Hess, S., Cecconi, B., & Zarka, P. (2008). Modeling of Io-Jupiter decameter arcs, emission beaming and energy source. *Geophysical Research Letters*, *35*(13). https://doi.org/10.1029/2008gl033656

Hess, S., Mottez, F., & Zarka, P. (2007). Jovian s burst generation by Alfvén waves. *Journal of Geophysical Research*, *112*(A11). https://doi.org/10.1029/2006JA012191

Hilgers, A. (1992). The auroral radiating plasma cavities. *Geophysical Research Letters*, *19*(3), 237–240. https://doi.org/10.1029/91gl02938

Hilgers, A., Roux, A., & Lundin, R. (1991). Characteristics of AKR sources; a statistical description. *Geophysical Research Letters*, *18*(8), 1493–1496. https://doi.org/10.1029/91gl01332

Knight, S. (1973). Parallel electric fields. *Planetary and Space Science*, *21*(5), 741–750. https://doi.org/10.1016/0032-0633(73)90093-7

Kotsiaros, S., Connerney, J. E. P., Clark, G., Allegrini, F., Gladstone, G. R., Kurth, W. S., et al. (2019). Publisher correction: Birkeland currents in Jupiter's magnetosphere observed by the polar-orbiting Juno spacecraft. *Nature Astronomy*, *3*(11), 1029. https://doi.org/10.1038/s41550-019-0938-1

Kurth, W. S. (2021). Juno e/j/s/ss waves calibrated burst full resolution v2.0 [dataset]. *NASA Planetary Data System*. https://doi.org/10.17189/1522461

Kurth, W. S., Hospodarsky, G. B., Kirchner, D. L., Mokrzycki, B. T., Averkamp, T. F., Robison, W. T., et al. (2017). The Juno waves investigation. *Space Science Reviews*, *213*(1), 347–392. https://doi.org/10.1007/s11214-017-0396-y

Lamy, L., Prangé, R., Tao, C., Kim, T., Badman, S., Zarka, P., et al. (2018). Saturn's northern aurorae at solstice from HST observations coordinated with Cassini's grand finale. *Geophysical Research Letters*, *45*(18), 9353–9362. https://doi.org/10.1029/2018gl078211

Le Queau, D., & Louarn, P. (1989). Analytical study of the relativistic dispersion: Application to the generation of the auroral kilometric radiation. *Journal of Geophysical Research*, *94*(A3), 2605–2616. https://doi.org/10.1029/JA094iA03p02605

Louarn, P., Allegrini, F., McComas, D. J., Valek, P. W., Kurth, W. S., André, N., et al. (2017). Generation of the Jovian hectometric radiation: First lessons from Juno. *Geophysical Research Letters*, *44*(10), 4439–4446. https://doi.org/10.1002/2017GL072923

Louarn, P., Allegrini, F., McComas, D. J., Valek, P. W., Kurth, W. S., André, N., et al. (2018). Observation of electron conics by Juno: Implications for radio generation and acceleration processes. *Geophysical Research Letters*, *45*(18), 9408–9416. https://doi.org/10.1029/2018GL078973

Louarn, P., Roux, A., de Féraudy, H., Le Quéau, D., André, M., & Matson, L. (1990). Trapped electrons as a free energy source for the auroral kilometric radiation. *Journal of Geophysical Research*, *95*(A5), 5983–5995. https://doi.org/10.1029/JA095iA05p05983

Louis, C. K., Louarn, P., Allegrini, F., Kurth, W. S., & Szalay, J. R. (2020). Ganymede-induced decametric radio emission: In situ observations and measurements by Juno. *Geophysical Research Letters*, *47*(20), e2020GL090021. https://doi.org/10.1029/2020GL090021

Louis, C. K., Prangé, R., Lamy, L., Zarka, P., Imai, M., Kurth, W. S., & Connerney, J. E. P. (2019). Jovian auroral radio sources detected in situ by Juno/waves: Comparisons with model auroral ovals and simultaneous HST FUV images. *Geophysical Research Letters*, *46*(21), 11606–11614. https://doi.org/10.1029/2019GL084799

Louis, C. K., Zarka, P., Cecconi, B., & Boudouma, A. (2023). Juno/waves estimated flux density collection. *PADC*. https://doi.org/10.25935/FWTQ-V202

Louis, C. K., Zarka, P., Dabidin, K., Lampson, P.-A., Magalhães, F. P., Boudouma, A., et al. (2021). Latitudinal beaming of Jupiter's radio emissions from Juno/waves flux density measurements. *Journal of Geophysical Research: Space Physics*, *126*(10), e2021JA029435. https://doi.org/10.1029/2021JA029435

Mauk, B. H., Clark, G., Gladstone, G. R., Kotsiaros, S., Adriani, A., Allegrini, F., et al. (2020). Energetic particles and acceleration regions over Jupiter's polar cap and main aurora: A broad overview. *Journal of Geophysical Research: Space Physics*, *125*(3), e2019JA027699. https://doi.org/10.1029/2019JA027699

Mauk, B. H., Haggerty, D. K., Paranicas, C., Clark, G., Kollmann, P., Rymer, A. M., et al. (2017). Juno observations of energetic charged particles over Jupiter's polar regions: Analysis of monodirectional and bidirectional electron beams. *Geophysical Research Letters*, *44*(10), 4410–4418. https://doi.org/10.1002/2016gl072286

McComas, D. J., Alexander, N., Allegrini, F., Bagenal, F., Beebe, C., Clark, G., et al. (2017). 11 01). The Jovian auroral distributions experiment (jade) on the Juno mission to Jupiter. *Space Science Reviews*, *213*(1), 547–643. https://doi.org/10.1007/s11214-013-9990-9

Menietti, J., Mutel, R., Schippers, P., Ye, S.-Y., Gurnett, D. A., & Lamy, L. (2011). Analysis of Saturn kilometric radiation near a source center. *Journal of Geophysical Research*, *116*(A12). https://doi.org/10.1029/2011ja017056

Mottez, F., & Génot, V. (2011). Electron acceleration by an Alfvénic pulse propagating in an auroral plasma cavity. *Journal of Geophysical Research*, *116*(A1). https://doi.org/10.1029/2010ja016367

Mutel, R. L., Menietti, J. D., Gurnett, D. A., Kurth, W., Schippers, P., Lynch, C., et al. (2010). Cmi growth rates for Saturnian kilometric radiation. *Geophysical Research Letters*, *37*(19). https://doi.org/10.1029/2010GL044940

Mutel, R. L., Peterson, W., Jaeger, T., & Scudder, J. (2007). Dependence of cyclotron maser instability growth rates on electron velocity distributions and perturbation by solitary waves. *Journal of Geophysical Research*, *112*(A7). https://doi.org/10.1029/2007ja012442

Ning, H., Chen, Y., Li, C., Ye, S., Kuznetsov, A., & Wu, S. (2023). Excitation of extraordinary modes inside the source of Saturn's kilometric radiation. *Astronomy & Astrophysics*, *678*, A94. https://doi.org/10.1051/0004-6361/202347149

Pritchett, P. L. (1984). Relativistic dispersion and the generation of auroral kilometric radiation. *Geophysical Research Letters*, *11*(2), 143–146. https://doi.org/10.1029/GL011i002p00143

Pritchett, P. L., Strangeway, R. J., Carlson, C. W., Ergun, R. E., McFadden, J. P., & Delory, G. T. (1999). Free energy sources and frequency bandwidth for the auroral kilometric radiation. *Journal of Geophysical Research*, *104*(A5), 10317–10326. https://doi.org/10.1029/1998ja900179

Roux, A., Hilgers, A., De Feraudy, H., Le Queau, D., Louarn, P., Perraut, S., et al. (1993). Auroral kilometric radiation sources: In situ and remote observations from Viking. *Journal of Geophysical Research*, *98*(A7), 11657–11670. https://doi.org/10.1029/92ja02309

Salveter, A., Saur, J., Clark, G., & Mauk, B. H. (2022). Jovian auroral electron precipitation budget—A statistical analysis of diffuse, mono-energetic, and broadband auroral electron distributions. *Journal of Geophysical Research: Space Physics*, *127*(8), e2021JA030224. https://doi.org/10.1029/2021JA030224

Sulaiman, A. H., Mauk, B. H., Szalay, J. R., Allegrini, F., Clark, G., Gladstone, G. R., et al. (2022). Jupiter's low-altitude auroral zones: Fields, particles, plasma waves, and density depletions. *Journal of Geophysical Research: Space Physics*, *127*(8), e2022JA030334. https://doi.org/10.1029/2022JA030334

Treumann, R. A. (2006). The electron–cyclotron maser for astrophysical application. *Astronomy and Astrophysics Review*, *13*(4), 229–315. https://doi.org/10.1007/s00159-006-0001-y

Wilson, R. J. (2020). Juno j/sw Jovian auroral distribution calibrated v1.0 [dataset]. NASA Planetary Data System. https://doi.org/10.17189/1519715

Wong, H., Wu, C., Ke, F., Schneider, R., & Ziebell, L. (1982). Electromagnetic cyclotron-loss-cone instability associated with weakly relativistic electrons. *Journal of Plasma Physics*, *28*(3), 503–525. https://doi.org/10.1017/s0022377800000453

Wu, C. (1985). Kinetic cyclotron and synchrotron maser instabilities: Radio emission processes by direct amplification of radiation. *Space Science Reviews*, *41*(3–4), 215–298. https://doi.org/10.1007/bf00190653

Wu, C. S., & Lee, L. C. (1979). A theory of the terrestrial kilometric radiation. *The Astrophysical Journal*, *230*, 621–626. https://doi.org/10.1086/157120

Zarka, P. (1998). Auroral radio emissions at the outer planets: Observations and theories. *Journal of Geophysical Research*, *103*(E9), 20159–-20194. https://doi.org/10.1029/98JE01323

Zarka, P., Farges, T., Ryabov, B. P., Abada-Simon, M., & Denis, L. (1996). A scenario for Jovian s-bursts. *Geophysical Research Letters*, *23*(2), 125–128. https://doi.org/10.1029/95GL03780

Zarka, P., Le Quéau, D., & Genova, F. (1986). The maser synchrotron instability in an inhomogeneous medium: Determination of the spectral intensity of auroral kilometric radiation. *Journal of Geophysical Research*, *91*(A12), 13542–13558. https://doi.org/10.1029/ja091ia12p13542